Nature Communications

https://doi.org/10.1038/s41467-026-69383-3

Article in Press

Hybrid macrophage-mitochondria extracellular vesicles for mitochondrial ROS regulation in diabetic wounds

Received: 21 July 2025

Accepted: 30 January 2026

Cite this article as: Fan, L., Zhang, C., Xu, Z. *et al.* Hybrid macrophage-mitochondria extracellular vesicles for mitochondrial ROS regulation in diabetic wounds. *Nat Commun* (2026). https://doi.org/10.1038/s41467-026-69383-3

Li Fan, Changhe Zhang, Zhigang Xu, Zhelong Li, Bin Zhang, Heng Li, Jingxiang Wang, Zhao Wei, Juntao Han, Hao Guan, Bo Peng, Nicolas H. Voelcker & Xuekang Yang

Hybrid macrophage-mitochondria extracellular vesicles for mitochondrial ROS regulation in diabetic wounds

Li Fan[1,#], Changhe Zhang[2,#], Zhigang Xu[1], Zhelong Li[3], Bin Zhang[3], Heng Li[1], Jingxiang Wang[1], Zhao Wei[4], Juntao Han[1], Hao Guan[1], Bo Peng[5,*], Nicolas H. Voelcker[2,6,7,*], Xuekang Yang[1,*]

[1]Department of Burns and Cutaneous Surgery, Xijing Hospital, The Fourth Military Medical University, Xi'an 710032, China.

[2]Monash Institute of Pharmaceutical Sciences, Monash University, Parkville, VIC, 3052, Australia.

[3]Department of Ultrasound Diagnostics Tangdu Hospital, The Fourth Military Medical University Xi'an 710038, China.

[4]School of Pharmacy, The Fourth Military Medical University, Xi'an, 710032, China. [5]State Key Laboratory of Flexible Electronics (LoFE) & Institute of Flexible Electronics (IFE), Northwestern Polytechnical University, Xi'an 710072, China.

[6]Melbourne Centre for Nanofabrication, Victorian Node of the Australian National Fabrication Facility, Clayton, VIC, 3168, Australia.

[7]Materials Science and Engineering, Monash University, Clayton, Victoria, 3168, Australia.

[#]These authors contributed equally.

*Address correspondence to: iambpeng@nwpu.edu.cn (B.P.); nicolas.voelcker@monash.edu (N.H.V.); sskzzb06@fmmu.edu.cn (X.K.Y.).

Abstract

Precise regulation of mitochondrial reactive oxygen species (mtROS) in macrophages is essential for reducing inflammation and promoting diabetic wound healing. However, achieving targeted and responsive mtROS modulation in specific cell remains challenging. Herein, we report a macrophage-mitochondria hybrid membrane derived artificial extracellular vesicle platform (C@AH-EV). C@AH-EV integrates biomimetic dual-targeting membranes with an mtROS activatable prodrug. It leverages membrane protein-mediated targeting of macrophage mitochondria to offer highly selective intracellular delivery. The payload is a ROS sensitive antioxidant prodrug, which incorporates lipid tails that enhance its drug loading efficiency in vesicles. Upon mtROS-triggered cleavage of the boronate ester bond, potent antioxidants were locally released within the mitochondria to restore redox balance. In vitro and in vivo studies demonstrate that C@AH-EVs effectively reprogram macrophages from an inflammatory toward an anti-inflammatory phenotype, thereby attenuating inflammation and accelerating diabetic wound repair. This work offers a promising direction for treating chronic inflammatory conditions.

Introduction

Impaired wound healing driven by diabetes is becoming a global concern, affecting 18.6 million people worldwide and posing a significant challenge to global healthcare system[1]. Current treatments for diabetic wounds include aggressive debridement, antibiotic medication, and revascularization[2-4]. However, these strategies often fall short of complete effectiveness. Statistics indicated that more than half of diabetic wounds still persist after three months of treatment[5], leading to potential amputation. Additionally, individuals with diabetic foot ulcers face a one-year mortality risk of 23%, comparable to that of cancer[6]. Therefore, there is an urgent need to develop more effective therapies for the treatment of diabetic wounds.

Macrophages, as the predominant inflammatory cells in a high-glycemic microenvironment, are recognized as key drivers of inflammation that contribute to non-healing diabetic wounds[7,8]. Under normal wound conditions, macrophages transition from the inflammatory M1-like phenotype to the anti-inflammatory M2-like phenotype. However, in a high-glucose microenvironment, excessive production of mitochondrial reactive oxygen species (mtROS) results in mitochondria dysfunction by damaging various molecular components, including DNA, lipids, proteins, and carbohydrates. Consequently, the transformation of macrophages from an M1-like to an M2-like phenotype is severely disrupted, hindering proper wound healing[9-11]. While scavenging mtROS can alleviate mitochondrial dysfunction, moderate levels of mtROS are essential for activating antioxidant pathways and promoting M2-like macrophage polarization, therefore, precisely modulating mtROS levels in macrophages is crucial for promoting diabetic wound healing[12,13].

To accomplish this goal, our primary task was to develop a smart macrophage mtROS modulation system, which remains a significant pharmacological challenge. In our previous study, we achieved preliminary success in macrophage mtROS modulation by combining mitochondrial-targeting elements with natural extracellular vesicle (EV)[14]. However, EV-based therapeutics still face challenges of low yield and heterogeneity[15]. In recent years, nanovesicles constructed by cell membrane and subcellular organelle membranes have attracted growing attention. These

nanovesicles exhibit a striking resemblance to EVs in size, morphology, and protein composition, and are thus widely regarded as artificial EVs[16]. They offer the distinct advantages of being more amenable to large-scale production and efficiently encapsulating diverse types of therapeutic agents, making them excellent substitutes for natural EVs[17]. Importantly, artificial EVs exhibit targeting capabilities since they retain structural and biological information about the donor cells or subcellular organelles[18,19]. Thus, cell and mitochondrial hybrid membrane based artificial EVs hold great potential for dual-targeting to both the cells and their mitochondria. But such hybrid membrane-derived vesicles remain unreported.

In terms of effective yet controllable scavenging of mtROS, covalent conjugation of antioxidants with ROS-responsive linkers offers a well-established strategy. Caffeic acid (CA) and its phenethyl ester (CAPE), natural phenylpropanoids with potent antioxidant activity[20,21], contain ortho-dihydroxyphenyl (catechol) groups that readily form dynamic boronic acid esters with phenylboronic acid derivatives[22]. However, direct conjugation often results in poor aqueous stability, limiting their utility for precise ROS modulation[23,24]. Anslyn *et al.* reported a robust, irreversible three-component reaction in aqueous media involving 2-formylphenylboronic acid, catechols, and N-alkyl hydroxylamines[25], an approach now recognized as a form of click chemistry due to its efficiency and simplicity[22,26]. Applying this strategy to conjugate CA/CAPE with boronic acids enables the construction of water-stable, ROS-responsive prodrugs.

As a result, we synthesised the prodrugs via three-component click reactions of CA or its phenyl ethyl ester CAPE with 2-formylphenyl boronic acid (2-FPBA) and *N*-dodecyl hydroxylamine (DO-HA), denoted as CAPE-FPBA-DO and CA-PFBA-DO, respectively. Among them, CAPE-FPBA-DO exhibited higher stability in aqueous solution and lower cytotoxicity. The dodecyl moiety of CAFE-FPBA-DO is designed to enhance drug hydrophobicity, enabling high-efficiency payload encapsulation via membrane adsorption[27,28]. By loading CAPE-FPBA-DO into artificial EVs derived from macrophage-mitochondria hybrid membrane, we engineered a macrophage mtROS on-demand scavenging nanovesicle, referred to as C@AH-EV (artificial hybrid membrane extracellular vesicle loaded with CAPE-FPBA-DO) (Fig. 1a). When applied to in vitro inflammatory cell models and in vivo diabetic wound mouse models, C@AH-EVs were taken up by macrophages through calthrin- and lipid raft-mediated endocytosis. Subsequently, these vesicles targeted the mitochondria via mitofusin (MFN) and fused with the mitochondrial membrane to release antioxidant prodrugs. In the presence of high levels of mtROS, CAPE-FPBA-DO degraded to release the potent antioxidants CAPE, which improved the mitochondria function by eliminating excessive mtROS, thereby reprogramming macrophage phenotypes and accelerating diabetic wound healing (Fig. 1b-c). This study presents a mitochondria-targeted, cell-specific nanotherapeutic that mimics endogenous communication mechanisms, providing a robust and precise mtROS scavenging strategy for wound healing and broader therapeutic application.

Results

Synthesis and analysis of ROS responsive/scavenging prodrugs.

To construct ROS responsive/scavenging prodrugs, we covalently conjugated caffeic acid (CA) or its phenyl ethyl ester (CAPE) with 2-formylphenyl boronic acid (2-FPBA) and *N*-dodecyl hydroxylamine (DO-HA) via three-component click reactions, denoted as CAPE-FPBA-DO and CA-FPBA-DO, respectively (Supplementary Fig.1, 2). The conjugates are anticipated to enable

on-demand release of CAPE/CA in response to different ROS levels (Fig. 2a)[23]. Their successful syntheses were confirmed by nuclear magnetic resonance (NMR) spectroscopy (Supplementary Fig.3-10) and UV-Vis analysis (Fig. 2b, c). To assess their drug-likeness, a structure-property relationship analysis was performed using Oprea's rules[29]. The results indicated that the ratio of CAPE-FPBA-DO and CA-FPBA-DO are as follow: the number of rings 5/4 (for CAPE-FPBA-DO and CA-FPBA-DO, respectively), the number of rigid bonds 30/25, the number of rotatable bonds 17/13, all of which are acceptable according to Oprea's rules (Supplementary Table 1). Then, we evaluated the cytotoxicity of CAPE-FPBA-DO and CA-FPBA-DO using the CCK-8 assay. The results showed that CAPE-FPBA-DO exhibit the significantly lower cytotoxicity compared to CA-FPBA-DO, with IC_{50} values of 106.6 μM for CAPE-FPBA-DO and 28.95 μM for CA-FPBA-DO (Fig. 2d). This may be attributed to its ester moiety for their modulation of pharmacokinetic parameters[30,31]. We next conducted stability analyses on CAPE-FPBA-DO and CA-FPBA-DO. UV-Vis analysis indicated that CA-FPBA-DO undergoes significant hydrolysis at concentrations near the non-cytotoxic level (25 μM), whereas CAPE-FPBA-DO exhibits relatively good hydrolytic stability at this concentration (Fig. 2e, Supplementary Fig. 11).

Studies have shown that mitochondrial dysfunction can lead to a significant increase in mtROS concentration, with localized levels (e.g., in the mitochondrial matrix) reaching up to 1 mM[32]. Thus, we investigated the ROS responsive behavior of CAPE-FPBA-DO and CA-FPBA-DO under varying H_2O_2 levels. High-performance liquid chromatography (HPLC) results showed released CAPE/CA and by-products at different retention times and UV absorption wavelengths, indicating that H_2O_2 triggered the decomposition of CAPE-FPBA-DO and CA-FPBA-DO (Supplementary Fig. 12, 13). The extent of drug release was concentration dependent, with values for CAPE and CA rising from 51.32% and 37.14% at 0.1 mM H_2O_2 to 77.77% and 74.47% at 1 mM H_2O_2 after 480 min of incubation (Fig. 2f, g, Supplementary Fig. 14, 15). These results confirm the potential on-demand release capabilities of CAPE-FPBA-DO and CA-FPBA-DO in dysfunctional mitochondrial environments. Notably, CAPE-FPBA-DO exhibited a slightly higher release capacity than CA-FPBA-DO during the 480 min detection period. This divergence may be attributed to the greater propensity of CA-FPBA-DO to form micellar aggregates in aqueous environments, which sequester the reactive boronic ester groups within a hydrophobic core, thereby shielding them from H_2O_2 solution and attenuating the reaction-driven release[33] (Supplementary Fig. 16). Subsequently, $ABTS^{\bullet+}$ (2,2'-azino-bis (3-ethylbenzothiazoline-6-sulfonic acid) diammonium salt radical cation) was incubated with the CAPE, CA, 2-FPBA, CAPE-FPBA-DO, or CA-FPBA-DO alone to assess the ROS scavenging ability (Fig. 2h). The results showed that CAPE and CA possessed comparable antioxidant capacity. Notably, CAPE/CA-FPBA-DO also decolorized $ABTS^{\bullet+}$ to some extent, which may be attributed to the production of ROS in the generation of $ABTS^{\bullet+}$ (Fig. 2i) [34,35].

In summary, both CAPE-FPBA-DO and CA-FPBA-DO demonstrating rapid responsiveness to ROS and effective ROS scavenging capabilities. Compared to CA-FPBA-DO, CAPE-FPBA-DO showed higher hydrolytic stability and lower cytotoxicity, making it a more promising antioxidant prodrug.

Construction and characterization of on-demand mitochondrial ROS scavenging nanovesicles

Next, we prepared artificial hybrid membrane extracellular vesicles (AH-EVs) to load the prodrug CAPE-FPBA-DO (Fig. 3a). Briefly, macrophage membrane (MM) and mitochondrial membrane (MitoM) from RAW 264.7 cells and its mitochondria were collected via membrane

lysis and subsequently purified. AH-EVs were formed using the ultrasonic approach followed by extrusion to control vesicles size. CAPE-FPBA-DO was loaded into AH-EVs through a co-incubation and extrusion process to prepare C@AH-EVs (AH-EVs loaded with CAPE-FPBA-DO). The successful fusion of MM and MitoM was confirmed by confocal laser scanning microscopy (CLSM) (Fig. 3b). Scanning electron microscope (SEM) images revealed the spherical morphology of the AH-EVs and C@AH-EVs (Fig. 3c), while transmission electron microscopy (TEM) images displayed a single membrane of phospholipid bilayer for both AH-EVs and C@AH-EVs (Fig. 3d).

To further investigate the membrane protein retention of C@AH-EVs, sodium dodecyl sulfate-polyacrylamide gel electrophoresis (SDS-PAGE) was performed. As shown in Supplementary Fig. 17, the protein profiles of C@AH-EVs were similar to those of AH-EVs, indicating good retention of MM and MitoM proteins. Furthermore, western blot analysis confirmed the presence of the internal reference of cell membranes Na^+/K^+ ATPase, macrophage membrane protein F4/80, and mitochondria membrane protein Bcl-2 in C@AH-EVs, suggesting that the membrane of C@AH-EVs was comparable to those on macrophage and mitochondria (Fig. 3e). Then the nanovesicles were further characterized by means of nanoparticle tracking analysis (NTA) and dynamic light scattering (DLS). The NTA showed that C@AH-EVs had an average size of 196 nm, which is similar to AH-EVs (197 nm) (Fig. 3f). In addition, there was no significant difference in the negative zeta potential between AH-EVs and C@AH-EVs (Fig. 3g). The drug loading capacity is crucial for determining the final therapeutic effect. Therefore, we utilized the highest safe concentration of 1 μM CAPE-FPBA-DO for C@AH-EVs preparation, achieving a 69% encapsulation efficiency for CAPE-FPBA-DO and a loading capacity of 403 ng/10^{10} particles (Fig. 3h, Supplementary Fig. 18). Subsequent CCK-8 assays and histological analysis further confirmed the biosafety of the prepared C@AH-EVs (Supplementary Fig. 19-21). Furthermore, C@AH-EVs maintained size stability for at least 72 h in both PBS and RPMI medium (Fig. 3i).

C@AH-EVs efficiently targeted the mitochondria of macrophage in vitro and in vivo.

Targeted delivery to mitochondria of macrophage is crucial for mtROS responding and scavenging. To this end, we first evaluated the cellular uptake of both DiI-labeled C@AH-EVs and C@AM-EVs (prepared by MM) by RAW 264.7 cells. The results indicated that the DiI signals in macrophages treated with C@AM-EVs and C@AH-EVs were similar. Additionally, we stimulated macrophages with lipopolysaccharide (LPS) to induce M1-like macrophages. In LPS-stimulated macrophages, we observed comparable uptake efficiency for both C@AM-EVs and C@AH-EVs. These results indicate that the addition of mitochondrial membranes did not affect the uptake efficiency of macrophages (Supplementary Fig. 22).

To further investigate mitochondrial homologous targeting of C@AH-EVs, MitoTracker (magenta) and DiO (green) were used (Fig. 4a). RAW 264.7 cells with C@AH-EVs produced enhanced white fluorescence resulting from the overlap of magenta and green, whereas RAW 264.7 cells treated with C@AM-EVs did not produce marked white fluorescence. Co-localization line scanning profiles also supported this conclusion, suggesting that the mitochondria membrane is necessary for mitochondria targeting. Furthermore, C@AH-EVs demonstrated favorable

targeting in the mitochondria of macrophages stimulated with LPS (Fig. 4b, c). These results suggest that the mitochondrial targeting of C@AH-EVs is membrane potential-independent, compensating for the limitations of membrane potential-dependent targeting elements like lipophilic cations[36].

In the subsequent experiment, we observed the mitochondrial targeting properties of C@AH-EVs in macrophages within diabetic wounds using CLSM (Supplementary Fig. 23). As shown in Figure 4d and Figure 4e, C@AH-EVs effectively targeted mitochondria of macrophages in both common and diabetic wounds. Notably, a small quantity of C@AH-EVs could potentially be internalized by other phagocytes and parenchymal cells. This is beneficial for wound treatment, as overproduction of mtROS in other cell types also contributes delayed wound healing[37,38]. Together, these data suggest that C@AH-EVs exhibits highly efficient and precise mitochondrial targeting in macrophages, holding significant superiority compared to membrane potential-dependent mitochondrial targeting materials.

Mechanism of cellular uptake and mitochondria targeting

Next, we elucidated the molecular mechanism underlying membrane-mediated homotypic recognition and delivery. Trypsin, a serine protease that can digest membrane proteins, was used to treat the MM for 6 h at 37℃, generating AH-EVs deficient in MM proteins, denote as C@AH-EVs$^{MM\ trypsin}$ (Supplementary Fig. 24). CLSM images showed that the uptake of C@AH-EVs$^{MM\ trypsin}$ by RAW 264.7 cells were decreased compared to the C@AH-EVs group (Fig. 5a, b). Similarly, C@AH-EVs$^{MitoM\ trypsin}$, deficient in MitoM protein, exhibited reduced co-localization with mitochondria (Supplementary Fig. 25, Fig. 5c-e), confirming that certain membrane proteins play critical roles in homotypic targeting.

We next used various blockers of specific cellular endocytosis pathways to investigate the mechanisms underlying C@AH-EVs internalization. The endocytosis pathways can be categorized into four types: macro-pinocytosis, lipid raft-mediated endocytosis (LrME), clathrin-mediated endocytosis (CME), and caveolae-mediated endocytosis (CvME)[39]. Thus amiloride (5-(N, N-dimethyl)-amiloride hydrochloride, inhibitor for macro-pinocytosis), MβCD (methyl-β-cyclodextrin, inhibitor of LrME), CPZ (chlorpromazine hydrochloride, inhibitor of CME), and Gen (genistein, inhibitor of CvME) were utilized to pretreat the RAW 264.7 cells (Fig. 5f). The CLSM images revealed the significant reduction in macrophage uptake of MβCD-treated group and CPZ-treated group, with uptake levels decreasing to 52.8% and 66.2% of the control group, respectively (Fig. 5g, h). Lipid rafts require membrane proteins (e.g., integrins) as functional anchors, critical for membrane localization[40]. CME is associated with signals from transmembrane receptors, a specialized class of membrane-embedded proteins[41]. Therefore, these results further demonstrate the potential of membrane proteins in the homotypic cell targeting. Additionally, the uptake of C@AH-EVs in RAW 264.7 cells incubated at 4°C dropped to 4.5% of control levels, which is likely associated with suppressed cellular energy metabolism and the reduction in membrane fluidity induced by low temperature[42].

As highly dynamic organelles, mitochondria possess remarkable membrane fusion capabilities. Consequently, nanoparticles prepared from mitochondrial membranes are highly

likely to exhibit similar characteristics, which subsequently detected by a mitochondria-nanovesicle fusion assay (Fig. 5i). In Figure 5j and 5k, we observed that the membrane of C@AH-EVs were fused with the outer mitochondrial membranes (OMM). In contrast, C@AM-EVs prepared with solely RAW 264.7 cell membranes did not fuse with mitochondria. Studies have shown that the fusion of the OMM is mediated by the dynamin-like protein mitofusin (MFN)[43]. The small molecule MFI8, which inhibits this process by binding MFN's HR2 domain, was utilized to investigate subcellular targeting mechanisms. The results showed that mitochondria pretreated with MFI8 were unable to fuse with C@AH-EVs, indicating that MFN is involved in mitochondrial targeting (Fig. 5j, k). This is consistent with previous study[44]. Altogether, these results suggest that membrane proteins are an important basis for homotypic targeting.

C@AH-EVs improve mitochondrial function by eliminating mtROS.

To further evaluate the therapeutic efficacy of C@AH-EVs, we first quantified CAPE release within macrophage mitochondria using HPLC, comparing LPS-stimulated macrophages with PBS controls. The results exhibited obvious increased mitochondrial CAPE accumulation in LPS-stimulated macrophages relative to PBS controls ($p < 0.05$), indicating that elevated mtROS concentrations effectively triggered boronate ester bond cleavage and promoted CAPE release (Supplementary Fig. 26). Then LPS-stimulated macrophages were divided into four treatment groups: PBS, AH-EVs, CAPE-FPBA-DO, and C@AH-EVs, with untreated macrophages serving as the control. mtROS levels were quantified using MitoSOX™ Red. As depicted in the Figure 6a and 6b, the mtROS level in the C@AH-EVs group was remarkably diminished compared to the PBS group, while the mtROS level in the AH-EVs group remained relatively unchanged. This phenomenon was primarily attributed to the antioxidant CAPE released by CAPE-FPBA-DO. In addition, although a slight visual decrease in mtROS was observed in cells treated with CAPE-FPBA-DO, this change was not statistically significant. This results further confirming that C@AH-EVs specifically target mtROS scavenging.

Functionally, excessive mtROS triggers mitochondrial lipid peroxidation, compromises membrane stability, leads to abnormal mitochondrial morphology, and disrupt ATP synthesis. Therefore, MitoPerOX was used to detect mitochondrial lipid peroxidation. The results revealed that C@AH-EVs significantly suppressed LPS-induced mitochondrial lipid peroxidation (Fig. 6c). To further evaluate the impact of mtROS on mitochondrial membrane potential ($\Delta\psi m$), we performed JC-1 staining. JC-1 accumulates in mitochondria in a potential-dependent manner, forming J aggregates (red) when inside. Conversely, upon mitochondrial depolarization, JC-1 persists as monomers (green) (Fig. 6d). The results demonstrated that LPS treatment induced $\Delta\psi m$ depolarization, as indicated by enhanced green fluorescence from JC-1 monomers. When treated with C@AH-EVs, cells exhibited increased red fluorescence from J-aggregates, indicating that C@AH-EVs effectively restored the $\Delta\psi m$ (Fig. 6e, Supplementary Fig. 27). It is noteworthy that CAPE-FPBA-DO, despite exhibiting antioxidant activity, demonstrated lesser regulatory effects on mitochondrial lipid peroxidation and $\Delta\psi m$ than C@AH-EVs.

The effect of C@AH-EVs on mitochondrial morphology was observed by electron microscopy. In normal cells, the mitochondrial cristae were distinctly visible and elongated. Upon

LPS treatment, the mitochondria underwent significant swelling and vesicular cristae, while C@AH-EVs administration significantly attenuated the damaged morphology (Fig. 6f, g). For ATP production, C@AH-EVs treatment resulted in a 2.72-fold, 2.94-fold, and 1.77-fold improvement compared with PBS, AH-EVs, and CAPE-FPBA-DO treatments, respectively (Fig. 6h). Taken together, these results suggests that C@AH-EVs have the capacity to improve mitochondrial function by effectively scavenging mtROS (Fig. 6i).

In vitro orchestration of macrophage phenotype by C@AH-EVs

Considering the regulatory effect of mitochondria on macrophage activation, we speculated that C@AH-EVs would modulate mitochondria-dependent macrophage activation. Subsequently, the phenotype of LPS-stimulated macrophages treated with PBS, AH-EVs, CAPE-FPBA-DO, and C@AH-EVs was analyzed by flow cytometry assay (Fig. 7a). As expected, C@AH-EVs demonstrated an inhibitory effect on CD86, a marker for M1-like macrophages (Fig. 7b). Additionally, qRT-PCR results showed that C@AH-EVs inhibited the expression of proinflammatory genes including *Tnfα*, *Nos2*, *Il6*, and *Cxcl1* (Fig. 7c). Given the necessity of M2-like macrophages for anti-inflammatory responses and diabetic wound healing, we assessed the effect of C@AH-EVs on M2-like macrophage activation by co-administering them with Interleukin-4 (IL-4), a key inducer of M2-like macrophage polarization (Fig. 7d). The results showed that IL-4 and C@AH-EVs synergistically upregulated expression of CD206, a hallmark of M2-like macrophages, in LPS-stimulated macrophages (Fig. 7e), suggesting a conversion from an M1-like to an M2-like phenotype. Furthermore, these cells exhibited obvious upregulation of the anti-inflammatory genes including *Arg1*, *Mrc1*, *Ym1*, and *Fizz1* (Fig. 7f).

In contrast, AH-EVs did not effectively regulate the genes and surface markers related to M1-like or M2-like phenotypes mentioned above in RAW 264.7 cells. Notably, while CAPE-FPBA-DO suppressed the expression of CD86 and inflammatory gene, and induced the expression of CD206 and anti-inflammatory genes, their effectiveness were reduced compared with C@AH-EVs. Altogether, these results indicate that C@AH-EVs can effectively regulate the phenotype of macrophages.

Besides, we also prepared hybrid membrane vesicles loaded with an equivalent mass of CAPE (CAPE@AH-EVs) as a control to evaluate the potential advantages of C@AH-EVs. The results demonstrated that whereas both AH-EVs effectively attenuated mtROS levels and reduced the proportion of M1-like macrophages, only C@AH-EVs significantly promoted M2-like macrophage polarization (Supplementary Fig. 28, 29). This discrepancy is likely attributable to the excessive scavenging of mtROS by CAPE@AH-EVs, which may obliterate the physiological levels of mtROS essential for driving M2-like macrophage polarization.

C@AH-EVs promote the M2-like macrophage polarization in vivo

The wound healing process consists of three stages: the inflammatory stage, the proliferative stage, and the remodeling stage. The inflammatory stage, typically lasting 2-3 days post-injury but often chronically prolonged in diabetic wounds, is characterized by sustained elevation of proinflammatory factors mediated through excessive M1-like macrophage polarization. Therefore,

we initially assessed the capability of C@AH-EVs to scavenge mtROS in macrophages and orchestrate macrophage phenotypes within a diabetic mouse full-thickness wound model.

First, the diabetic wound model was created by injecting streptozotocin at a dose of 50 mg kg^{-1} day^{-1} for 5 days, followed by surgical removal of 10-mm-diameter full-thickness skin after consistent blood glucose levels over 16.65 mmol L^{-1} for one week. The persistent hyperglycemia and impaired weight gain collectively demonstrate that the mice maintained a sustained diabetic state throughout the experimental period (Supplementary Fig. 30). Subsequently, PBS, AH-EVs, CAPE-FPBA-DO, and C@AH-EVs were subcutaneously administrated at the wound sites, respectively. Tracking of DiI-labeled C@AH-EVs exhibited an efficient distribution throughout the full thickness of the wound tissue (Supplementary Fig. 31). Considering the prolonged inflammation associated with diabetic wounds, in vivo macrophage mtROS levels and macrophage phenotypes were determined on the day 3, 7, and 14 (Supplementary Fig. 32). Macrophages were gated using the markers F4/80 and CD11b (Supplementary Fig. 33). With in the $CD11b^+$ $F4/80^+$ macrophage population, the expression level of mtROS, CD86, and CD206 were evaluated.

The results showed that in diabetic mouse model with full-thickness skin defect, mtROS levels and the proportion of proinflammatory M1-like macrophages in wound tissues exhibited a persistent high-state throughout the observation period. Upon intervention with C@AH-EVs in diabetic wounds, the mtROS levels decreased to 32.4%, 22.6%, and 26.4% on day 3, 7, and 14, respectively (Fig. 8a, c, e). Concurrently, the proportion of M1-like macrophages decreased to 43.1% at day 3, 38.1% at day 7, and 19.1% at day 14, while the proportion of M2-like macrophages, which are associated with tissue repair, increased to 39.7%, 56.9%, and 72.2% at the respective timepoints (Fig. 8b, d, f, Supplementary Fig. 34). ELISA analysis of cytokines further validated the macrophage phenotypic shift, showing a reduction in proinflammatory cytokines and an elevation in anti-inflammatory cytokines across all time points. Specifically, levels of TNF-α and IL-1β in the C@AH-EV-treated group were lower than those in the control group at each time point (Supplementary Fig. 35). Conversely, the anti-inflammatory cytokines TGF-β and IL-10 were significantly increased (Supplementary Fig. 36). In contrast, the AH-EV group demonstrated unresolved inflammation, characterized by a failure to downregulate $CD86^+$ macrophages and persistently high levels of proinflammatory cytokines. While CAPE-FPBA-DO exhibited some capacity of macrophage phenotypic regulation, its overall therapeutic efficacy in wound repair is significantly inferior to that of C@AH-EVs. These results suggest that C@AH-EVs-mediated suppression of mtROS levels promotes a microenvironment conducive to M2-like macrophage activation.

C@AH-EVs enhance diabetic wound healing in full-thickness skin defect model

We next investigated the therapeutic effects of C@AH-EVs in diabetic wounds (Fig. 9a). Representative macroscopic wound images (Fig. 9b), along with the wound closure traces at different time intervals (Fig. 9c), and the corresponding quantitative data (Fig. 9d, Supplementary Fig. 37) collectively demonstrate the enhanced therapeutic efficacy of C@AH-EVs. On day 5, the wounds in the C@AH-EVs group were noticeably smaller compared to those in the other groups. By day 10, a remarkable reduction in the wound area was observed in the C@AH-EVs group,

achieving a wound healing rate of 78.2%. In contrast, the wounds healing rate in the control group, AH-EVs group, and CAPE-FPBA-DO group remained at 58.6%, 58.8%, and 68.3%, respectively. On day 14, the C@AH-EVs-treated diabetic wounds showed substantial healing (86.3% wound healing rates), while the control group, AH-EVs group, and CAPE-FPBA-DO group exhibited persistently lower healing rates (72.9%, 75.5%, 77.7%, respectively).

H&E staining was performed to investigate the histological changes in wounds. On day 3, the inflammatory cells in the wounds of the C@AH-EVs group were significantly lower than those in the other three groups, with no epidermal formation observed in any group (Fig. 9e, Supplementary Fig. 38). By day 7, the C@AH-EVs group exhibited epidermal regeneration, while the other groups did not show this progression. On day 14, all groups completed re-epithelialization and displayed mature stratified epithelial cells. However, the regeneration of skin appendages, such as hair follicles and sebaceous glands was the most pronounced in the C@AH-EVs group. Organized formation of granulation tissue further substantiated its therapeutic superiority in wound healing (Fig. 9e, Supplementary Fig. 39).

Neovascularization is a key characteristic during the proliferative stage of wound healing. During tissue repair, M2-like macrophages regulate the expression and function of platelet endothelial cell adhesion molecule-1 (CD31) in endothelial cells by secreting vascular endothelial growth factor (VEGF), thereby stimulating the formation of new blood vessels and accelerating wound healing. Therefore, during the proliferative phase, immunostaining of CD31 and VEGF was performed to evaluate neovascularization in the granulation tissue. As shown in Supplementary Figure 40, the wound sections from the C@AH-EVs group exhibiting the highest level of CD31 and VEGF, with the relative coverage areas of VEGF and CD31 being 5.59 times and 3.80 times higher compared to the PBS group, respectively. This suggests that C@AH-EVs hold great potential in facilitating wound healing by augmenting angiogenesis.

Proper collagen deposition and remodeling during the remodeling phase are vital for restoring wound biomechanics. Thus, we employed Masson's trichrome staining to evaluate collagen architecture in this critical stage. As shown in Supplementary Fig. 41, the C@AH-EVs group displayed denser collagen fibers with a collagen volume fraction of 51.86%. In contrast, the PBS group, AH-EVs group, and CAPE-FPBA-DO group had lower collagen volume fractions of 39.56%, 40.95%, and 40.67%, respectively. These fibers demonstrated a more mature phenotype characterized by well-organized alignment and an intricate collagen network topology, especially in comparison to the PBS and AH-EVs group. These results verified the improved collagen deposition ability of C@AH-EVs.

Besides, macrophage membrane-derived artificial EVs (AMM-EVs), mitochondria membrane-derived artificial EVs (AMitoM-EVs), CAPE, CAPE@AH-EVs, and clinically used agent Beifuji were also served as controls to evaluate the therapeutic efficacy of C@AH-EVs. The results demonstrated that diabetic wounds treated with C@AH-EVs exhibited accelerated healing than other groups (Supplementary Fig. 42). Consistent with this, the C@AH-EVs group formed more mature granulation tissue, accompanied by accelerated re-epithelialization, skin appendage regeneration, and neovascularization relative to all controls (Supplementary Fig. 43). In summary, C@AH-EVs can effectively accelerate the healing process of diabetic wounds.

Discussion

Targeting the clearance of mtROS in macrophages is an effective approach to promote wound healing. Although numerous mitochondrial-targeting strategies such as small-molecule compounds and synthetic nanoparticles have been developed, their translational application value is significantly limited due to inefficiencies in targeted delivery systems, poor intracellular drug stability, and potential toxicity risks to healthy tissue. Importantly, most existing systems focus solely on scavenging mtROS, which may lead to excessive depletion of physiological mtROS levels and thereby inhibit M2-like macrophage polarization. This study effectively addresses these challenges by integrating macrophage-mitochondrial hybrid membrane vesicles with ROS-responsive prodrugs. The vesicles not only exhibit an improved safety profile but, more importantly, achieve specific delivery to macrophage mitochondria, independently of the mitochondrial membrane potential. Furthermore, its nano-encapsulation capability protects the prodrug from degradation, thereby ensuring the attainment of effective local drug concentrations. Upon internalization into the macrophage mitochondria, the prodrug CAPE-FPBA-DO were released and exhibits mtROS concentration-dependent antioxidant activity. This mechanism not only exerts anti-inflammatory effects but also maintains mtROS at a lower, homeostatic level, thereby preventing the impairment of M2-like macrophage polarization caused by excessive mtROS scavenging.

It is worth mentioning that, theoretically, CAPE-FPBA-DO can be taken up by macrophages to exert anti-inflammatory effects by responding and scavenging cytoplasmic ROS. However, the therapeutic efficacy of CAPE-FPBA-DO was notably inferior to that of C@AH-EVs, which may be attributed to premature drug release and a lack of mitochondrial targeting capability. Although CAPE@AH-EVs can effectively scavenge mtROS, their excessive clearance impairs M2-like macrophage polarization. These results further highlight the importance of mitochondria-targeted therapy and mtROS on-demand scavenging, particularly for applications such as diabetic wound healing. Besides, macrophages possess various types of receptors on their cell membrane surfaces, such as toll-like receptors, integrin receptors, and scavenger receptors. These receptors can mitigate inflammation by competitively binding to DAMPs or chemokines[45]. However, in this study, AH-EVs and AMM-EVs did not exhibit an obvious anti-inflammatory trend. This discrepancy may be attributed to the reduced surface area of macrophage membranes in the AH-EVs and suboptimal drug dosage.

Our results indicate that the targeting capability of C@AH-EVs is closely associated with membrane proteins, a property potentially achieved through collaborative or independent mechanisms. Toward macrophages targeting, it is achieved through the CME and LrME, suggesting that proteins associated with these pathways may serve as key mediators in homologous targeting. Regarding mitochondrial targeting, we have verified a strong association with mitofusin (MFN), but it is unclear whether this involves synergy with other proteins. Consequently, the specific contributions and functional interplay of these proteins require further experimental validation.

As mimics of EVs, C@AH-EVs inherently lack sufficient tissue penetration capability. While the subcutaneous injection approach has yielded promising results in our study, non-invasive

therapeutic strategies (such as hydrogels and wound dressings) hold greater potential for clinical application due to their improved feasibility and patient compliance. Therefore, in our subsequent research, we will focus on enhancing the tissue penetration depth of these nanomaterials by employing more efficient delivery vehicles to accelerating their translation into clinical practice. Furthermore, although CAPE-FPBA-DO demonstrates good hydrolytic stability at lower concentrations, it still potentially exhibits concentration dependence. While encapsulation within AH-EVs offers a degree of protection, the semi-permeable nature of the lipid bilayer membrane still allows small molecules such as ions to potentially enter the vesicles through diffusion or channel-mediated transport, thereby exposing the prodrug to more complex physiological conditions. Hence, elucidating their in vivo behavior will enable a more efficient path toward clinical translation.

In summary, we developed a drug delivery system capable of precise clearance of mtROS in macrophages. The application of this system to diabetic full-thickness wounds significantly promoted wound healing. And this approach also holds broad therapeutic potential for inflammatory diseases caused by mitochondrial redox dysregulation.

Methods

Ethical regulations

All experiments were authorized by the Animal Care and Ethic Committee of Fourth Military Medical University (Approval NO. IACUC-20240917).

Materials

All organic solvents were used as received. CA, CAPE and 2-FBPA were purchased from Ambeed USA. Dodecyl aldehyde, hydroxyamine hydrochloride, pyridine borane complex and acetyl chloride were purchased from Sigma Aldrich Australia. 2,2'-azinobis-(3-ethylbenzothiazoline-6-sulfonate) (ABTS) kits were obtained from Yuanye Bio-Technology (China). Mitochondria isolation kit, cell counting kit-8 (CCK-8), MitoTracker Deep Red^{FM}, and ATP assay kit were purchased from Beyotime Biotechnology (China). RPMI (Roswell Park Memorial Institute) and fetal bovine serum were purchased from Excell Bio (China). Penicillin streptomycin was supplied by Solarbio (China). 3,3'-Dioctadecyloxacarbocyanine perchlorate (DiO), 1,1'-dioctadecyl-3,3,3',3'-tetramethylindocarbocyanine perchlorate (DiI), Hoechst 33342, 4′,6-diamidino-2-phenylindole (DAPI), MitoSOX^{TM}, and JC-1 were purchased from Invitrogen (US). MitoPerOx, MFI8 was supplied by MedChemExpress (US). Amiloride (5-(N,N-dimethyl)-amiloride hydrochloride), MβCD (methyl-β-cyclodextrin, 5 mM), Gen (genistein), and CPZ (chlorpromazine) were purchased from Sigma-Aldrich (China). Mouse ELISA kits were obtained from Elabscience (China). Antibodies used in flow cytometry: FITC-conjugated Rat Anti-Mouse CD86 (105006), PE-conjugated Rat Anti-Mouse CD206 (141706), and APC-conjugated Rat Anti-Mouse F4/80 (123116) were purchased from Biolegend (US), PerCP-conjugated Rat Anti-Mouse CD11b (E-AB-F1081F) was purchased from Elabscience (China). Antibodies used in western blot: rabbit anti-F4/80 (29414-1-AP), rabbit anti-Bcl-2 (26593-1-AP), rabbit anti-Na^+/K^+ ATPase (14418-1-AP) were obtained from Proteintech (China). Antibodies used in immunofluorescence and immunohistochemistry: rabbit anti-Tom20 (11802-1-AP) was purchased from Proteintech

(China), rabbit anti-F4/80 (GB113373), rabbit anti-CD31 (GB15063), and rabbit anti-VEGF (GB15165) were purchased from Servicebio (China).

Cell lines and animals

The murine cell line RAW 264.7 was obtained from the American Type Culture Collection (TIB-71, ATCC). Cells were cultured in RPMI medium supplemented with the 10% FBS and 1% antibiotics at 37℃, 5% CO_2. Cells were changed with fresh medium every other day. BALB/c mice (male, 8-10 weeks) were obtained from the Animal Center of Fourth Military Medical University. All mice were housed at a constant temperature and humidity in a room with an artificial 12 h light/dark cycle and allowed free access to water and diet. The animal experimental procedures were performed strictly following the guidelines approved by the Institutional Animal Experiment Administration Committee of the Fourth Military Medical University.

Synthesis of CAPE-FPBA-DO and CA-FPBA-DO

*(E, Z)-Dodecanal oxime **S2***: Hydroxylamine hydrochloride (2.8 g, 40 mmol) was dissolved in a NaOH solution in water (4 N, 12 mL) and the resulted solution was added to dodecylaldehyde **S1** solution (17.5 mmol in 15 mL EtOH). The mixture was heated at 70 ºC overnight. After cooling to room temperature, water (30 mL) was added to the mixture resulting in precipitation. Solid was collected by filtration to get an off-white solid as a mixture of isomers (*E*/*Z* 1:0.8, 86% yield).

*N-dodecylhydroxylamine **S3***: In one flask, to MeOH (5 mL) was added AcCl (12.5 mmol, 0.9 mL) at 0ºC under N_2. After stirring for 10 min, the generated HCl solution in MeOH was added to a solution of oximes (5 mmol) and pyridine borane complex (Py·BH_3, 2.2 equiv., 11 mmol) in MeOH dropwise at 0ºC via syringe. The reaction was stirred for 5 h at rt followed by quenching with Na_2CO_3 solutions. The mixture was then extracted with EtOAc (40 mL × 3) and then the combined organic phase was washed with brine. After drying over $MgSO_4$, the solution was filtered and concentrated before purification via flash chromatography. The title compound was obtained as a white solid (75% yield).

CAPE-FPBA-DO: To the suspension of CAPE (1.0 mmol) and 2-FPBA (1.0 mmol) in $CHCl_3$ (5 mL) was added hydroxyamine **S3** (1.05 mmol) powder, the reaction was stirred at rt for 15 min as it turned bright yellow. The mixture was then loaded to a column packed with silica (230–400 mesh) and eluted with acetone. The yellow fractions were collected and concentrated to obtain a bright yellow solid (83% yield).

CA-FPBA-DO: To the suspension of CA (1.0 mmol) and 2-FPBA (1.0 mmol) in $CHCl_3$ (5 mL) was added hydroxyamine **S3** (1.05 mmol) powder, the reaction was stirred at rt for 15 min as it turned bright yellow. The mixture was then loaded to a column packed with silica (230–400 mesh) and eluted with acetone. The yellow fractions were collected and concentrated to get yellow solids (78% yield).

IC_{50} assay of CAPE-FPBA-DO and CA-FPBA-DO to RAW 264.7 cells

The IC_{50} (half-maximal inhibitory concentration) assay was analyzed by CCK-8 as instructed. Briefly, 5×10^3 RAW 264.7 cells were seeded in 96-well plates and cultured for 12 h. Subsequently, the media were replaced with fresh media containing different concentrations of CAPE-FPBA-DO and CA-FPBA-DO, respectively. After incubation for another 24 h, replaced the medium and added 10 ul CCK-8 to each well. Absorbance at 450 nm was measured using a microplate reader

(Tecan infinite M200 Pro, Switzerland) after 1 h.

Stability assay

The complexes (CAPE-FPBA-DO and CA-FPBA-DO) used for the testing were dissolved in the mixture of PBS /DMSO (8:2 *v/v*) with 0.5% (*w/v*) surfactant. UV-vis spectra were recorded for determining the stability of the complexes.

Synthesis of SA-DO

Dodecyl hydroxylamine (402 mg, 2 mmol) and salicylaldehyde (244 mg, 2 mmol) were mixed in dichloromethane (5 mL). The mixture was stirred overnight at rt before purification via flash chromatography over silica gel. The compound was isolated as a white solid.

ROS-responsive of CAPE-FPBA-DO and CA-FPBA-DO

To determine the ROS-responsive ability of CAPE-FPBA-DO and CA-FPBA-DO, the in vitro drug release tests were evaluated in the absence/presence of H_2O_2 conditions. Specifically, the CAPE-FPBA-DO and CA-FPBA-DO were incubated with PBS (pH = 7.4, 0.1 M) or H_2O_2 (0.1 mM H_2O_2, 1 mM H_2O_2) at 37 ℃ with orbital shaking at about 100 rpm. At specified time intervals (0, 40, 80, 120, 240, 480 min), the solution was withdrawn and replaced with the same volume of fresh media. The released CAPE and CA were determined by high performance liquid chromatography (ACQUITY UPLC H-Class waters, US).

ABTS free radical scavenging analysis

The antioxidant activity of CAPE, CA, 2-FPBA, CAPE-FPBA-DO, and CA-FPBA-DO were assessed by the 2,2'- azinobis-(3-ethylbenzothiazoline-6-sulfonate) (ABTS) radical scavenging assays and quantified by microplate reader. Specifically, the working solution is prepared by mixing ABTS (7 mM) and potassium persulfate (2.45 mM) solutions in a 1:1 ratio, followed by incubation in the dark at room temperature (25°C) for 12 h. Then the solution was diluted 30-fold and combined with CAPE, CA, 2-FPBA, CAPE-FPBA-DO, and CA-FPBA-DO at varying concentrations (0, 0.025, 0.05, 0.10, 0.20, 0.40 mM). After incubation in the dark for 30 min, the values of OD samples and OD control were measured using a microplate reader at 734 nm. The ABTS radical scavenging ratios were obtained using the following formulae:

$$\text{ABTS ROS scavenging ratio (\%)} = (\text{OD control} - \text{OD sample})/\text{OD control} \times 100\%$$

Preparation of macrophage and mitochondria membrane

Macrophage membrane (MM) fragments collected from RAW 264.7 cells. Briefly, RAW 264.7 cells were collected and suspended at a density of 2.0×10^7 cells mL^{-1} in hypotonic lysis buffer (pH 7.4, 10 mM Tris, 1 mM $MgCl_2$) containing Complete Tablets mini protease inhibitor and disrupted via homogenization with Dounce homogenizer (Sigma, US). Then the obtained mixture was centrifuged (700 g, 10 min, 4 °C) and further centrifuged (10,000 g, 10 min, 4 °C) to remove unbroken cells and organelles. Finally, the resulting supernatant was centrifugated at 100,000 g (70 min, 4 °C) to obtain the MM. The resulting membrane pellets were stored at − 80 °C for future study.

Mitochondria membrane (MitoM) was prepared through mitochondrial isolation and subsequent disruption of the mitochondria. In brief, the collected cells were resuspended in mitochondria

isolation buffer for 15 min at 4 ℃, then subjected to Dounce homogenization to break up the cells. Next, the cell homogenate was centrifuged at 11,000 × g for 10 min at 4 °C to obtain mitochondria. The MitoM was obtained via breaking up by lysis buffer and ultracentrifuging at 100,000 g, 4 °C for 70 min, which was stored at −80 °C for further use.

Preparation of AH-EVs and C@AH-EVs

Combine the MM solution and MitoM solution in a 1: 1 membrane protein mass ratio and the samples were sonicated putted into ultrasonic disrupter (Sonics, US) an ice water bath to facilitate membrane fusion (on 2 s/off 2 s, 5 min, 20% amplitude). Then the 5.8 μg CAPE-FPBA-DO was added into the hybrid membrane suspension (100 μg of membrane protein), followed by co-incubation for 30 minutes and subsequent sequential extruded through 800 nm, 400 nm, and 200 nm polycarbonate porous membranes using an Avanti mini extruder to facilitate drug-laden vesicle formation. The resulting hybrid membrane vesicles were subsequently isolated at 100,000 g (4 °C, 90 min) to remove the unencapsulated drugs, followed by PBS resuspension to acquire C@AH-EVs. While AH-EVs were generated under identical experimental conditions excluding drug administration.

Characterization of AH-EVs and C@AH-EVs

The membrane hybridization was characterized by confocal laser scanning microscopy (CLSM, Nikon A1R, Japan). Scanning electron microscopy (ThermoFisher Quattro S, US), transmission electron microscopy (JEM-2000 EX TEM, Japan), western blot, Nanoparticle Tracking Analysis (Particle Metrix, GER), and dynamic light scattering (Mastersizer 2000, Malvern, US) were performed to characterize AH-EVs and C@AH-EVs morphology, classic membrane markers (F4/80, Bcl-2, Na^+/K^+ ATPase), size distribution, and zeta potential. Loading capacity and encapsulation efficiency of CAPE-FPBA-DO were quantified by using HPLC. Encapsulation efficiency (EE) was calculated using the following formulae:

EE (%) = (Amount of CAPE-FPBA-DO in AH-EVs/Amount of total CAPE-FPBA-DO) × 100

In vitro and in vivo safety evaluation

In vitro cytotoxicity was assessed with RAW264.7 cells by CCK-8 assays as instructed. Briefly, 2×10^3 cells were seeded in 96-well plates. After incubation for 12 h, the media were replaced with fresh media containing PBS and C@AH-EVs (40 μg mL^{-1}), respectively. After incubation for another 24 h, replaced the medium and added 10 ul CCK-8 to each well. Absorbance at 450 nm was measured to quantify the cytotoxicity.

The biocompatibility of C@AH-EVs in vivo was also evaluated. Eight-week-old BALB/c mice were randomly divided into two groups receiving subcutaneous injections of either PBS or C@AH-EVs (100 μg cm^{-2}) around the wounds. Skin tissues were harvested after 3 days continuous injection. Major organs and blood samples were harvested from 14 days of continuous injection. Organ samples underwent hematoxylin and eosin (H&E) staining for histological assessment. Serum was collected from the blood for the measurement of biochemical markers (ALT, AST, Cr, CK).

In vitro cellular uptake and in vivo distribution of C@AH-EVs

The cellular uptake tests were conducted in RAW 264.7 cells (with or without LPS pretreated). The cells were incubated with C@AM-EVs and C@AH-EVs (labeled with DiI, red) for 12 h, respectively. Then the cells were washed with PBS for three times and subsequent counterstained with Hoechst (blue) for 15 min. After PBS washed again, the cells were observed via CLSM.

For mitochondrial localization studies, a similar protocol was used. Cells were incubated with C@AM-EVs and C@AH-EVs (labeled with DiO, green) for 12 h, then washed three times with PBS and sequentially stained with MitoTracker Deep Red^{FM} for mitochondria (magenta) and Hoechst for nuclei (blue), and finally visualized under CLSM. Image J software was used to calculate a Pearson's coefficient.

Immunofluorescence was used to analyze the in vivo distribution of C@AH-EVs. Specifically, normal and diabetic BALB/c mice were subcutaneously injected with DiI-labeled C@AH-EVs (red) at a dose of 100 μg cm^{-2} around the wound site. At 12 h post-injection, the mice were euthanized and skin tissues were harvested for fixation. The penetration depth of C@AH-EVs in vivo was observed using CLSM following DAPI staining. Besides, Cryosectioned specimens were subjected to triple immunofluorescence staining using anti-F4/80 antibody (macrophage marker, magenta), anti-TOM20 antibody (mitochondrial marker, green), and Hoechst (nuclear counterstain, blue). The in vivo biodistribution of C@AH-EVs was subsequently analyzed by CLSM. Image J software was used to calculate a Pearson's coefficient.

Endocytic pathway study of C@AH-EVs

The impact of membrane protein integrity on endocytic pathways was evaluated according to established trypsin digestion protocol[46]. Briefly, isolated macrophage membranes and mitochondrial membranes were separately incubated with 50 μg mL^{-1} trypsin at 37°C for 6 h, followed by C@AH-EVs constitution using the established membrane fusion methodology. Purified C@AH-EVs from both trypsin-treated and untreated groups were resuspended in PBS. After labeling C@AH-EVs with lipophilic fluorescent dyes (DiI for C@AH-EVs$^{MM\ trypsin}$, DiO for C@AH-EVs$^{MitoM\ \ trypsin}$), they were co-cultured with macrophages for 12 h. Cells were subsequently stained with Hoechst and MitoTracker Deep Red. C@AH-EVs internalization and mitochondrial co-localization were quantitatively analyzed by CLSM.

Pharmacological inhibitors were used to study endocytosis of C@AH-EVs. Briefly, RAW 264.7 cells were pretreated with amiloride (5-(N, N-dimethyl)-amiloride hydrochloride, 200 μM), MβCD (methyl-β-cyclodextrin, 5 mM), Gen (genistein, 200 μM), and CPZ (chlorpromazine, 10 μM) for 30 min, and 4 ℃ for 1 h, respectively. Subsequently, the cells were co-cultured with DiI-labeled C@AH-EVs for 12 h followed with Hoechst staining. Fluorescence images were acquired with CLSM.

In vitro fusion assay

To evaluate the mitochondrial uptake mechanism of C@AH-EVs, MFI8 (Mitochondrial Fusion Inhibitor 8) was utilized. In brief, mitochondria were isolated according to manufacturers' instructions, followed by treatment with MFI8 (20 μM) for 30 min. Then C@AH-EVs and mitochondria were mixed in equal amounts and incubated at 37°C for 60 min. Mitochondria treated with C@AM-EVs (lacking mitochondrial membrane components) served as the negative control. Mitochondria-nanovesicle interactions were then evaluated by TEM.

ROS-responsiveness of C@AH-EVs in mitochondria of RAW 264.7 cells

RAW 264.7 cells were incubated with media containing 100 ng mL^{-1} LPS and 40 μg mL^{-1} C@AH-EVs for 12 h. Subsequently, the cells were collected, and the mitochondria were isolated using mitochondria extraction kit. Prepared mitochondrial lysates, and the concentration of CAPE in mitochondria were detected by HPLC. RAW 264.7 cells treated with C@AH-EVs alone served as control.

Detection of mitochondrial reactive oxygen species

Mitochondrial reactive oxygen species (mtROS) were detected by MitoSOX. Briefly, RAW 264.7 cells were pretreated with 100 ng mL^{-1} LPS (lipopolysaccharide, typical ROS inducer) for 12 h and subsequently subjected to different treatments (PBS, AH-EVs, CAPE-FPBA-DO, C@AH-EVs). After 24 h of treatment, the culture medium was discarded and cells were incubated with 5 mM MitoSOX working solution at 37℃ for 20 min in the dark. Then cells were washed thrice with PBS and stained with Hoechst. mtROS were quantitatively analyzed by CLSM.

Mitochondria lipid peroxidation measurement

RAW 264.7 cells were seeded in 6-well plates and pretreated with LPS for 12 h. After treated with PBS, AH-EVs (40 μg mL^{-1}), CAPE-FPBA-DO (1 μM), C@AH-EVs (40 μg mL^{-1}) for 24 h, respectively, cells were harvested and incubated with 100 nM MitoPerOx for 30 min at room temperature. Mitochondria lipid peroxidation was evaluated using Beckman CytoFlex (US) and the data were analyzed with Flowjo VX software.

Detection of mitochondrial membrane Potential (ΔΨm)

Mitochondrial membrane potential (ΔΨm) was studied using the JC-1 fluorescence according to the manufacturer's instructions. Briefly, RAW 264.7 cells were cultured in 6-well plates and pretreated with LPS for 12 h. Then the cells were treated with PBS, AH-EVs, CAPE-FPBA-DO, C@AH-EVs for 24 h, respectively. Subsequently, cells were incubated with 1 mg mL^{-1} JC-1 at 37°C in the dark for 20 min. The fluorescence signals were analyzed by means of flow cytometry.

Detection of mitochondria structure

RAW 264.7 cells were cultured in 10 cm plates and pretreated with LPS for 12 h. After treated with PBS, AH-EVs, CAPE-FPBA-DO, C@AH-EVs for 24h, respectively, cells were fixed using 2.5% glutaraldehyde solution at 4℃ for 4 h followed by post-fixed in 1% osmium tetroxide solution at room temperature for 1 h. Then the cells were washed three times with PBS and dehydrated in a graded series of ethanol (50%, 70%, 90%, 95%, and 100%) to acetone and embedded in epoxy resin that was polymerized in 60℃ thermostats for 48 h. Then the cell blocks were cut into 70 nm thick ultrathin sections and dual-stained with 2% uranyl acetate and 0.4% lead citrate for 15 min at room temperature. The ultra-thin section was imaged and analyzed by TEM. Mitochondrial morphology was quantified by analyzing the length/width ratio of all mitochondria within three randomly selected cells per group.

ATP measurement

ATP levels were measured using ATP Assay Kit according to the manufacturer's instructions. Briefly, the collected cells were lysed with a lysis buffer and then centrifuged at 12000 g for 10 min at 4 ℃. The ATP content was determined by chemiluminescence of the supernatant using a microplate reader.

Evaluation of macrophage polarization in vitro

After treatment with PBS, AH-EVs, CAPE-FPBA-DO, and C@AH-EVs, RAW 264.7 cells cultured in 6-wells plate were harvested and incubated with fluorochrome-conjugated antibodies (M1-like macrophages were labeled with CD86-FITC, and M2-like macrophages were labeled with CD206-PE) for 30 min at 4°C. Then cells were washed twice with flow-cytometry buffer. The fluorescence signals were analyzed by flow cytometry and the data were analyzed with Flowjo VX software.

mRNA expression of proinflammatory genes (*Tnfα*, *Nos2*, *Il6*, and *Cxcl1*) and anti-inflammatory genes (*Arg1*, *Mrc1*, *Ym1*, and *Fizz1*) were performed by Quantitative PCR. Relative gene expression was normalized to β-actin quantified with the $2^{-\Delta\Delta Ct}$ method for comparison. The PCR primers were obtained from PrimerBank and synthesized by AuGCT Biotech. Their sequences are provided in Supplementary Table S2.

In vivo therapeutic efficacy study in diabetic wounds

A mouse model of diabetic wounds was created to evaluate the therapeutic efficacy. Male BALB/c mice (8-10 weeks) were fasted for 12 h, followed by a single intraperitoneal injection of 50 mg kg^{-1} streptozotocin for 5 consecutive days. Blood glucose levels were monitored after 7 days, and those exhibiting levels >16.65 mM were classified as diabetic. Subsequently, full thickness wounds were established by 10 mm-diameter skin biopsy punches.

After the diabetic wound model was established, mice were subcutaneously injected with PBS (100 μL), AH-EVs (100 μg), CAPE-FPBA-DO (100 μL of 1 μM), CAPE (100 μL of 1 μM), AMitoM- EVs (100 μg), AMM-EVs (100 μg), CAPE@AH-EVs (100 μg), Beifuji (100 μL), and C@AH-EVs (100 μg) around the wounds at 4 injection sites (25 μL per site). The healing process of the wounds were recorded by taking the digital images of wounds and the wound area was measured using Image J software.

At indicated time points, wound tissues were harvested and homogenized for assessing the macrophage mtROS levels and phenotypes using flow cytometry. Hematoxylin & eosin (H&E) and Masson's trichrome staining were performed to histopathological analysis. The levels of TNF-α, IL-1β, TGF-β, and IL-10 were determined through ELISA kits. Immunofluorescence staining was conducted to detect CD31 and VEGF expression.

Statistical analysis

All data are given as mean ± SD. Results were analyzed by GraphPad Prism software 10.1.2 and Microsoft Excel (2024). Two-tailed Student's t test was utilized for differences between two groups. One-way ANOVA with Tukey's multiple comparison test and Two-way ANOVA with Dunnett's multiple comparisons were utilized for statistical significance of multiple comparisons.

Data availability

The data that support the findings of this study are available within the article and its Supplementary Information files. Source data is available for Fig. 2d-g, Fig. 2i, Fig. 3e, Fig. 3g-i, Fig. 5b, Fig. 5h, Fig. 5k, Fig. 6b-c, Fig. 6g-h, Fig. 7b-c, Fig. 7e-f, Fig. 8a-f, Fig. 9d, Supplementary Fig. 16, Supplementary Fig. 19, Supplementary Fig. 21-22, Supplementary Fig. 26-30, Supplementary Fig. 34-43. Source data are provided with this paper.

References

1. Zhang, Y.*, et al.* Global Disability Burdens of Diabetes-Related Lower-Extremity Complications in 1990 and 2016. *Diabetes Care* **43**, 964-974 (2020).
2. Powers, J.G., Higham, C., Broussard, K. & Phillips, T.J. Wound healing and treating wounds: Chronic wound care and management. *J Am Acad Dermatol* **74**, 607-625 (2016).
3. Lipsky, B.A. A Current Approach to Diabetic Foot Infections. *Curr Infect Dis Rep* **1**, 253-260 (1999).
4. Osterman, F.A., Jr. The use of angioplasty, bypass surgery, and amputation in the management of peripheral vascular disease. *N Engl J Med* **326**, 414 (1992).
5. da Silva, A.F.*, et al.* The management and outcome of critical limb ischaemia in diabetic patients: results of a national survey. Audit Committee of the Vascular Surgical Society of Great Britain and Ireland. *Diabet Med* **13**, 726-728 (1996).
6. Saluja, S.*, et al.* Foot ulceration and its association with mortality in diabetes mellitus: a meta-analysis. *Diabet Med* **37**, 211-218 (2020).
7. Monaghan, M.G., Borah, R., Thomsen, C. & Browne, S. Thou shall not heal: Overcoming the non-healing behaviour of diabetic foot ulcers by engineering the inflammatory microenvironment. *Adv Drug Deliv Rev* **203**, 115120 (2023).
8. Li, M., Hou, Q., Zhong, L., Zhao, Y. & Fu, X. Macrophage Related Chronic Inflammation in Non-Healing Wounds. *Front Immunol* **12**, 681710 (2021).
9. Vikram, A., Tripathi, D.N., Kumar, A. & Singh, S. Oxidative stress and inflammation in diabetic complications. *Int J Endocrinol* **2014**, 679754 (2014).
10. Bullon, P., Newman, H.N. & Battino, M. Obesity, diabetes mellitus, atherosclerosis and chronic periodontitis: a shared pathology via oxidative stress and mitochondrial dysfunction? *Periodontol 2000* **64**, 139-153 (2014).
11. Puleston, D.J.*, et al.* Polyamines and eIF5A Hypusination Modulate Mitochondrial Respiration and Macrophage Activation. *Cell Metab* **30**, 352-363 e358 (2019).
12. Glorieux, C., Liu, S., Trachootham, D. & Huang, P. Targeting ROS in cancer: rationale and strategies. *Nat Rev Drug Discov* **23**, 583-606 (2024).
13. Formentini, L.*, et al.* Mitochondrial ROS Production Protects the Intestine from Inflammation through Functional M2 Macrophage Polarization. *Cell Rep* **19**, 1202-1213 (2017).
14. Fan, L.*, et al.* Exosome-Based Mitochondrial Delivery of circRNA mSCAR Alleviates Sepsis by Orchestrating Macrophage Activation. *Adv Sci* **10**, e2205692 (2023).
15. Wang, Y.A.-O.*, et al.* Extracellular vesicles from 3D cultured dermal papilla cells improve wound healing via Krüppel-like factor 4/vascular endothelial growth factor A -driven angiogenesis. *Burns Trauma* **30**, tkad034 (2023).
16. Wen, Y.*, et al.* Cell-derived nanovesicles prepared by membrane extrusion are good substitutes for natural extracellular vesicles. *Extracellular Vesicle* **1**, 100004 (2022).
17. Jang, S.C.*, et al.* Bioinspired exosome-mimetic nanovesicles for targeted delivery of chemotherapeutics to malignant tumors. *ACS Nano* **7**, 7698-7710 (2013).
18. Lai, J., Huang, C., Guo, Y. & Rao, L. Engineered extracellular vesicles and their mimics in cardiovascular diseases. *J Control Release* **347**, 27-43 (2022).
19. Gong, H.*, et al.* Nanomaterial Biointerfacing via Mitochondrial Membrane Coating for Targeted

Detoxification and Molecular Detection. *Nano Lett* **21**, 2603-2609 (2021).

20. Nakayama, T. Suppression of hydroperoxide-induced cytotoxicity by polyphenols. *Cancer Res* **54**, 1991s-1993s (1994).
21. Pavlíková, N. Caffeic Acid and Diseases-Mechanisms of Action. *Int J Mol Sci* **24**, 588 (2022).
22. Chatterjee, S., Anslyn, E.V. & Bandyopadhyay, A. Boronic acid based dynamic click chemistry: recent advances and emergent applications. *Chem Sci* **12**, 1585-1599 (2021).
23. Wang, P., Gong, Q., Hu, J., Li, X. & Zhang, X. Reactive Oxygen Species (ROS)-Responsive Prodrugs, Probes, and Theranostic Prodrugs: Applications in the ROS-Related Diseases. *J Med Chem* **64**, 298-325 (2020).
24. Larcher, A., Lebrun, A., Smietana, M. & Laurencin, D. A multinuclear NMR perspective on the complexation between bisboronic acids and bisbenzoxaboroles withcis-diols. *New J Chem* **42**, 2815-2823 (2018).
25. Meadows, M.K., Roesner, E.K., Lynch, V.M., James, T.D. & Anslyn, E.V. Boronic Acid Mediated Coupling of Catechols and N-Hydroxylamines: A Bioorthogonal Reaction to Label Peptides. *Org Lett* **19**, 3179-3182 (2017).
26. Kolb, H.C., Finn Mg Fau - Sharpless, K.B. & Sharpless, K.B. Click Chemistry: Diverse Chemical Function from a Few Good Reactions. *Angew Chem Int Ed Engl* **40**, 2004-2021 (2001).
27. Baker, P.J.*, et al.* Molecular structures that influence the immunomodulatory properties of the lipid A and inner core region oligosaccharides of bacterial lipopolysaccharides. *Infect Immun* **62**, 2257-2269 (1994).
28. Fahy, E.*, et al.* A comprehensive classification system for lipids. *J Lipid Res* **46**, 839-861 (2005).
29. Oprea, T.I. Property distribution of drug-related chemical databases. *J Comput Aided Mol Des* **14**, 251-264 (2000).
30. Dekant, W., Fujii, K., Shibata, E., Morita, O. & Shimotoyodome, A. Safety assessment of green tea based beverages and dried green tea extracts as nutritional supplements. *Toxicol Lett* **277**, 104-108 (2017).
31. C. Magnani, V.L.B.I., M. A. Correa and H. R. N. Salgado. Caffeic acid: a review of its potential use in medications and cosmetics. *RSC* **6**, 3203-3210 (2014).
32. Gandin, V., Khalkar, P., Braude, J. & Fernandes, A.P. Organic selenium compounds as potential chemotherapeutic agents for improved cancer treatment. *Free Radic Biol Med* **127**, 80-97 (2018).
33. Ghezzi, M.*, et al.* Polymeric micelles in drug delivery: An insight of the techniques for their characterization and assessment in biorelevant conditions. *J Control Release* **332**, 312-336 (2021).
34. Wacławek, S.*, et al.* Chemistry of persulfates in water and wastewater treatment: A review. *Chem Eng J* **330**, 44-62 (2017).
35. Wu, X.J.*, et al.* A catalyst-free co-reaction system of long-lasting and intensive chemiluminescence applied to the detection of alkaline phosphatase. *Mikrochim Acta* **189**, 181 (2022).
36. Zielonka, J.*, et al.* Mitochondria-Targeted Triphenylphosphonium-Based Compounds: Syntheses, Mechanisms of Action, and Therapeutic and Diagnostic Applications. *Chem Rev* **117**, 10043-10120 (2017).
37. Bock, F.A.-O. & Tait, S.A.-O.X. Mitochondria as multifaceted regulators of cell death. *Nat Rev Mol Cell Biol* **21**, 85-100 (2020).
38. Giacco, F. & Brownlee, M. Oxidative stress and diabetic complications. *Circ Res* **107**, 1058-1070 (2010).

39. Iversen, T.-G., Skotland, T. & Sandvig, K. Endocytosis and intracellular transport of nanoparticles: Present knowledge and need for future studies. *Nano Today* **6**, 176-185 (2011).
40. Leitinger, B. & Hogg, N. The involvement of lipid rafts in the regulation of integrin function. *J Cell Sci* **115**, 963-972 (2002).
41. McMahon, H.T. & Boucrot, E. Molecular mechanism and physiological functions of clathrin-mediated endocytosis. *Nat Rev Mol Cell Biol* **12**, 517-533 (2011).
42. Bag, N., Yap, D.H.X. & Wohland, T. Temperature dependence of diffusion in model and live cell membranes characterized by imaging fluorescence correlation spectroscopy. *Biochimica et Biophysica Acta (BBA) - Biomembranes* **1838**, 802-813 (2014).
43. Gao, S. & Hu, J. Mitochondrial Fusion: The Machineries In and Out. *Trends Cell Biol* **31**, 62-74 (2021).
44. Jiang, L., *et al.* Mitochondrion-specific dendritic lipopeptide liposomes for targeted sub-cellular delivery. *Nat Commun* **12**, 2390 (2021).
45. Gao, C., *et al.* Treatment of atherosclerosis by macrophage-biomimetic nanoparticles via targeted pharmacotherapy and sequestration of proinflammatory cytokines. *Nat Commun* **11**, 2622 (2020).
46. Choi, D., *et al.* Quantitative proteomic analysis of trypsin-treated extracellular vesicles to identify the real-vesicular proteins. *J Extracell Vesicles* **9**, 1757209 (2020).

Acknowledgements

This work was supported by National Natural Science Foundation of China (Grant No. 82402908 to L.F., Grant No. 82372523 J.T.H., Grant No. 62475216 to B.P., Grant No. 82272261 to X.K.Y.), Shaanxi Province Foundation of China (Grant No. 2025PT-03, 2024SF-ZDCYL-04-10 to H.G., Grant No. 2024GH-ZDXM-37 to B.P., Grant No. 2022JC-58, 2024SF-ZDCYL-03-26 to X.K.Y.).

Author contributions

L.F. and C.H.Z. collaborated to complete the study and drafted the manuscript. Z.G.X., Z.L.L., and B.Z. assisted with preparation of nanovesicles. H.L. and J.X.W. assisted with animal experiments. Z.W., J.T.H., and H.G. provided technique help for this study. B.P., N.H.V., and X.K.Y. reviewed and edited the manuscript. All authors discussed the results and implications, and commented on the paper.

Competing interests

The authors declare no competing interests.

Figure legends

Fig. 1 Design of on-demand mtROS scavenging artificial EVs for diabetic wound healing. **a** Preparation of C@AH-EVs. CAPE, phenylethyl caffeate. 2-FPBA, 2-formylphenyl boronic acid. DO-HA, *N*-dodecyl hydroxylamine. **b** C@AH-EVs accelerate diabetic wound healing by inducing M2-like macrophage polarization via on-demand scavenging of mtROS. **c** The potential mechanism by which C@AH-EVs target mitochondria to regulate macrophage phenotypes: (1) Clathrin- and lipid raft-mediated endocytosis. (2) Membrane tethering by mitofusin (MFN). (3) The fusion of mitochondria membrane and C@AH-EVs membrane promotes drug release. (4) CAPE-FPBA-DO releases CAPE in response to mtROS.

(5) Released CAPE improved mitochondrial function by scavenging mtROS. (6) Mitochondria-dependent polarization of M2-like macrophages.

Fig. 2 Synthesis and characterization of CAPE-FPBA-DO and CA-FPBA-DO. a Schematic illustration of ROS-triggered CAPE/CA release from CAPE/CA-FPBA-DO. **b** UV-Vis spectra of CAPE, 2-FPBA, DO (dodecylaldehyde), and CAPE-FPBA-DO. The UV-Vis spectra were representative data from three independent experiments. The UV-Vis spectra were representative data from three independent experiments. **c** UV-Vis spectra of CA, 2-FPBA, DO, and CA-FPBA-DO. The UV-Vis spectra were representative data from three independent experiments. **d** IC_{50} analysis of RAW 264.7 cells (n = 3 biologically independent samples). **e** Stability of 25 μM CAPE-FPBA-DO and CA-FPBA-DO in PBS monitored by UV-Vis absorption (n = 3 independent samples). **f, g** In vitro cumulative drug release from CAPE-FPBA-DO (0.5 mg mL^{-1}) and CA-FPBA-DO (0.5 mg mL^{-1}) with different concentration of H_2O_2 (0.1 mM and 1mM). PBS without H_2O_2 was served as control (n = 3 independent samples). **h** $ABTS^{\bullet+}$ reaction mechanisms with an antioxidant agent. **i** ROS scavenging activities of CAPE, CA, 2-FPBA, CAPE-FPBA-DO, and CA-FPBA-DO were assessed by ABTS assay (n = 3 independent samples). Data are presented as mean ± SD. One-way ANOVA with Tukey's multiple comparison test was used in (**f**) and (**g**). Source data are provided as a Source data file.

Fig. 3 Construction and characterization of C@AH-EVs. a Schematic illustration of preparation of C@AH-EVs. **b** Images of C@AH-EVs by confocal laser scanning microscopy (CLSM). Fusion between macrophage membrane (MM, labeled with DiO, green) and mitochondria membrane (MitoM, labeled with DiI, red) of C@AH-EVs shown by merged image with yellow fluorescence. Scale bar, 200 nm. The CLSM images were representative data from three independent experiments. **c** Scanning electron microscopy (SEM) images of AH-EVs and C@AH-EVs. Scale bar, 500 nm. The SEM images were representative data from three independent experiments. **d** Transmission electron microscopy (TEM) images of AH-EVs and C@AH-EVs. Scale bar, 500 nm. The TEM images were representative data from three independent experiments. **e** Characteristic protein bands of MM, MitoM, AH-EVs, and C@AH-EVs resolved by western blotting. The immunoblots were representative data from three independent experiments. **f** Respective size distribution of AH-EVs and C@AH-EVs. The size analysis were representative data from three independent experiments. **g** Zeta potential of AH-EVs and C@AH-EVs (n = 3 biologically independent samples). **h** Loading capacity and encapsulation efficiencies of C@AH-EVs (n = 3 biologically independent samples). **i** Diameter changes of C@AH-EVs placed in PBS and RPMI medium for 72 h, respectively (n = 3 biologically independent samples). Data are presented as mean ± SD. Two-tailed Student's t test was used in (**g**). Source data are provided as a Source data file.

Fig. 4 Co-localization of C@AH-EVs with mitochondria in macrophages in vitro and in vivo. a Schematic illustration of the experimental procedure. RAW 264.7 cells were incubated with DiO-labeled nanovesicles for 12 h, followed by immunofluorescence analysis. CLSM images (**b**) and co-localization analysis (**c**) showing the mitochondria localization of C@AM-EVs and C@AH-EVs. Areas with white fluorescence in the merged CLSM images denote the co-localization of the mitochondria and nanovesicles. The mitochondria were stained with MitoTracker deep red (magenta), and nuclei were stained with Hoechst

(blue). Scale bar, 5 μm. The CLSM images were representative data from three independent experiments. CLSM images (**d**) and co-localization analysis (**e**) showing the co-localization of C@AH-EVs with mitochondria in wound tissue macrophages. Magenta: F4/80, Green: Tom20, Red: DiI, Blue: Hoechst. Scale bar, 40 μm. Rr: Pearson correlation coefficient. The CLSM images were representative data from three mice. Source data are provided as a Source Data file.

Fig. 5 Mechanism underlying macrophage endocytosis and mitochondrial localization of C@AH-EVs. Representative CLSM images (**a**) and analysis (**b**) for macrophage uptake of DiI labeled nanovesicles. Red: DiI, Blue: Hoechst. Scale bar, 10 μm (n = 3 biologically independent samples). CLSM images (**c**) and co-localization analysis (**d**, **e**) showing mitochondrial localization of the nanovesicles. Areas with white fluorescence in the merged CLSM images denote the co-localization. The mitochondria were stained with MitoTracker deep red (magenta), and nuclei were stained with Hoechst (blue). Rr: Pearson correlation coefficient. Scale bar, 5 μm. The CLSM images were representative data from three independent experiments. **f** Schematic illustration of selective drug inhibitors for the endocytosis pathway. RAW 264.7 cells were incubated with DiI-labeled nanovesicles after selective pharmaceutical inhibitors pretreated. The cellular uptake of nanovesicles was observed using CLSM (**g**), and its fluorescence intensity was quantitatively analyzed (**h**). Red: DiI, Blue: Hoechst. Scale bar, 10 μm (n = 4 biologically independent samples). **i** Schematic illustration of the fusion assay. Mitochondria pretreated with PBS or MFI8 were co-incubated with the indicated nanovesicles at 37°C for 60 min. Representative TEM images (**j**) and fusion efficiency analysis (**k**) showed the fusion of mitochondria with nanovesicles. M, mitochondria; V, nanovesicles. Scale bars, 500 nm (n = 4 biologically independent samples). Data are presented as mean ± SD. Two-tailed Student's t test was used in (**b**), and one-way ANOVA with Tukey's multiple comparison test was used in (**h**) and (**k**). Source data are provided as a Source data file.

Fig. 6 C@AH-EVs modulate mitochondria function via mtROS scavenging. Representative CLSM images (**a**) and quantitative analysis (**b**) of MitoSOX fluorescence in RAW 264.7 cells treated with PBS, AH-EVs, CAPE-FPBA-DO, and C@AH-EVs for 24 h. Red: MitoSOX, Blue: Hoechst. Scale bar, 20 μm (n = 3 biologically independent samples). **c** Flow cytometry analysis of mitochondrial (Mito) lipid peroxidation in RAW 264.7 cells (n = 3 biologically independent samples). **d** Schematic illustration of JC-1 staining evaluating mitochondrial depolarization. JC-1 accumulates in mitochondria in a potential-dependent manner. Once inside, it begins to form J aggregates (red). Conversely, upon mitochondrial depolarization, JC-1 persists as a monomer (green). **e** Flow cytometry plots of JC-1 aggregates and monomer in RAW 264.7 cells treated with PBS, AH-EVs, CAPE-FPBA-DO, and C@AH-EVs. The flow cytometry plots were representative data from three independent experiments. **f** TEM images of mitochondrial ultrastructure in RAW 264.7 cells treated with PBS, AH-EVs, CAPE-FPBA-DO, and C@AH-EVs. Scale bar, 500 μm. **g** Statistical analysis of mitochondria length/width ratio in the different treatment groups (n = 55 (Ctrl), 52 (PBS), 56 (AH-EVs), 58 (CAPE-FPBA-DO), 60 (C@AH-EVs) mitochondria). **h** ATP levels in RAW 264.7 cells after treated with PBS, AH-EVs, CAPE-FPBA-DO, and C@AH-EVs (n = 3 biologically independent samples). **i** Schematic illustration of C@AH-EVs improving mitochondrial function in RAW 264.7 cells. Data are presented as mean ± SD. One-way ANOVA with Tukey's multiple comparison test was used in (**b**), (**c**), (**g**), and (**h**). Source data are provided as a Source

data file.

Fig. 7 C@AH-EVs orchestrate macrophage phenotype in vitro. a Schematic illustration of the experimental procedure. RAW 264.7 cells were stimulated with LPS for 12 h. Subsequently, the cells were treated with PBS, AH-EVs, CAPE-FPBA-DO, and C@AH-EVs for 24 h. Untreated macrophages served as control. **b** Flow cytometry analysis of $CD86^+$ macrophage (n = 3 biologically independent samples). **c** Relative mRNA expression of proinflammatory genes (*Tnfα*, *Nos2*, *Il6*, and *Cxcl1*) (n = 3 biologically independent samples). **d** Schematic illustration of the experimental procedure. RAW 264.7 cells were primed with LPS for 12 h. Subsequently, the cells were treated with PBS, AH-EV, CAPE-FPBA-DO, and C@AH-EVs (each combined with IL-4) for 24 h. Untreated macrophages served as control. **e** Flow cytometry analysis of $CD206^+$ macrophages (n = 3 biologically independent samples). **f** Relative mRNA expression of anti-inflammatory genes (*Arg1*, *Mrc1*, *Ym1*, and *Fizz1*) (n = 3 biologically independent samples). Data are presented as mean ± SD. One-way ANOVA with Tukey's multiple comparison test was used in (**b**), (**c**) (**e**) and (**f**). Source data are provided as a Source data file.

Fig. 8 C@AH-EVs promote M2-like macrophage polarization via mtROS scavenging in vivo. Flow cytometry analysis of mtROS contents in macrophages in diabetic wounds at day 3 (**a**), day 7 (**c**), and day 14 (**e**) after indicated treatment (n = 4 biologically independent samples). Analysis of the ratio of M2-like macrophages in diabetic wounds at day 3 (**b**), day 7 (**d**) and day 14 (**f**) after indicated treatment (n = 4 biologically independent samples). Data are presented as mean ± SD. One-way ANOVA with Tukey's multiple comparison test was used in (**a-f**). Source data are provided as a Source data file.

Fig. 9 C@AH-EVs accelerates wound closure in diabetic mice. a Schematic illustration of the experimental procedure for in vivo evaluation of C@AH-EVs therapeutic efficacy. Digital photos of wounds (**b**) and traces of wounds closure (**c**) in different groups during the treatment period. Scale bar, 5 mm. The digital photos were representative data from six biologically independent wounds. **d** Quantitative analysis of wound closure rate over time (n = 6 biologically independent wounds). **e** H&E images of the wound tissue treated as described above on day 3, day 7, and day 14. Scale bar, 1000 μm for the normal-sized image and 100 μm for the magnified image. The H&E images were representative data from four biologically independent wounds. Data are presented as mean ± SD. Two-way ANOVA with Dunnett's multiple comparisons was used in (**d**). Source data are provided as a Source data file.

Editor Summary:

Controlling mitochondrial ROS has potential to regulate inflammatory responses, however targeting macrophages can be difficult. Here, the authors create hybrid membrane extracellular vesicles capable of targeted delivery to macrophages to modulate mitochondrial ROS, promoting diabetic wound healing.

Peer Review Information:

Nature Communications thanks Yun Liu and the other anonymous reviewers for their contribution to the peer review of this work. [A peer review file is available.]

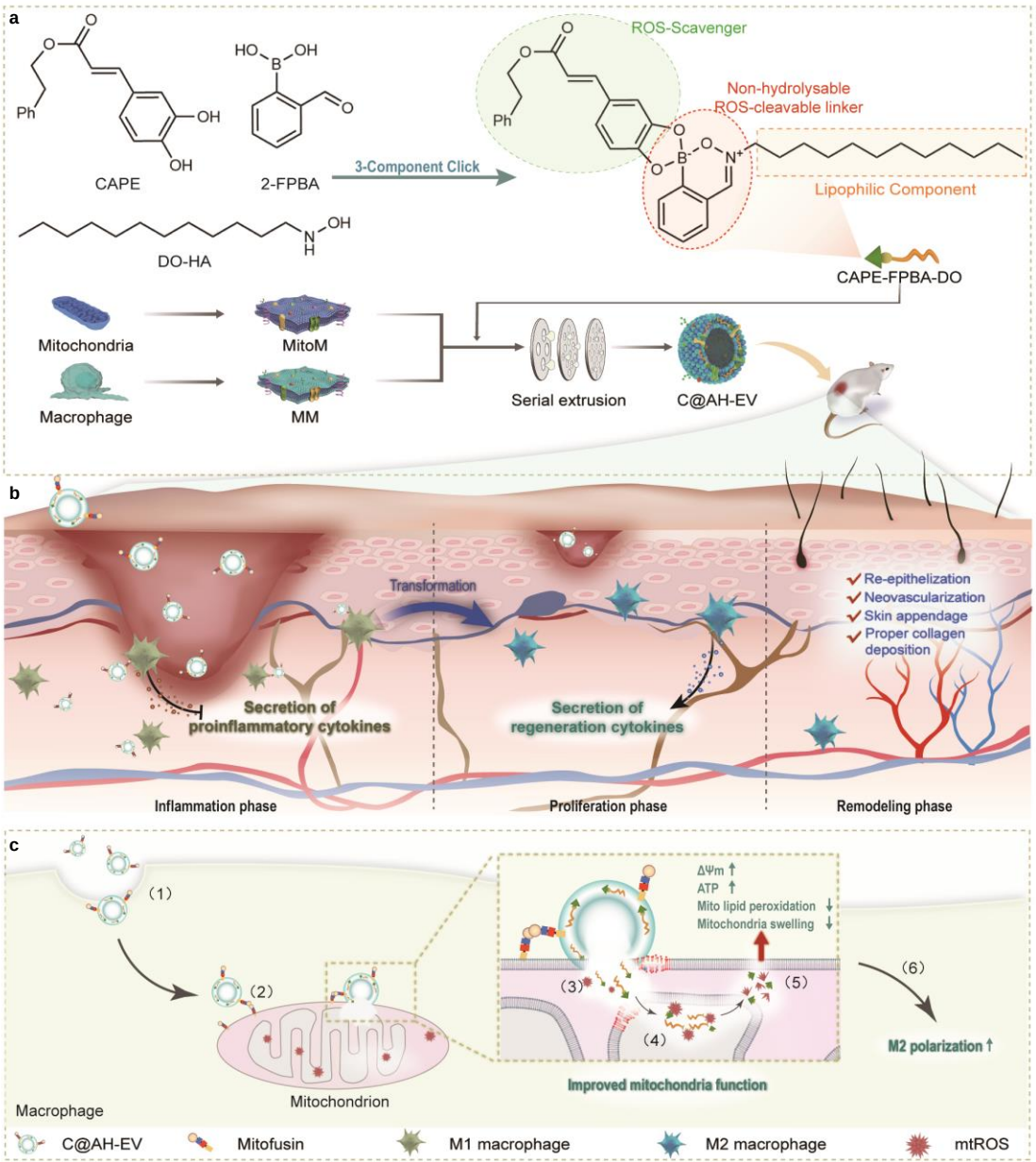
a
CAPE
2-FPBA
3-Component Click
ROS-Scavenger
Non-hydrolysable
ROS-cleavable linker
Lipophilic Component
DO-HA
CAPE-FPBA-DO
Mitochondria
MitoM
Macrophage
MM
Serial extrusion
C@AH-EV
b
Transformation
Re-epithelization
Neovascularization
Skin appendage
Proper collagen deposition
Secretion of proinflammatory cytokines
Secretion of regeneration cytokines
Inflammation phase
Proliferation phase
Remodeling phase
c
(1)
(2)
(3)
(4)
(5)
(6)
ΔΨm ↑
ATP ↑
Mito lipid peroxidation ↓
Mitochondria swelling ↓
Mitochondrion
Macrophage
Improved mitochondria function
M2 polarization ↑
C@AH-EV
Mitofusin
M1 macrophage
M2 macrophage
mtROS

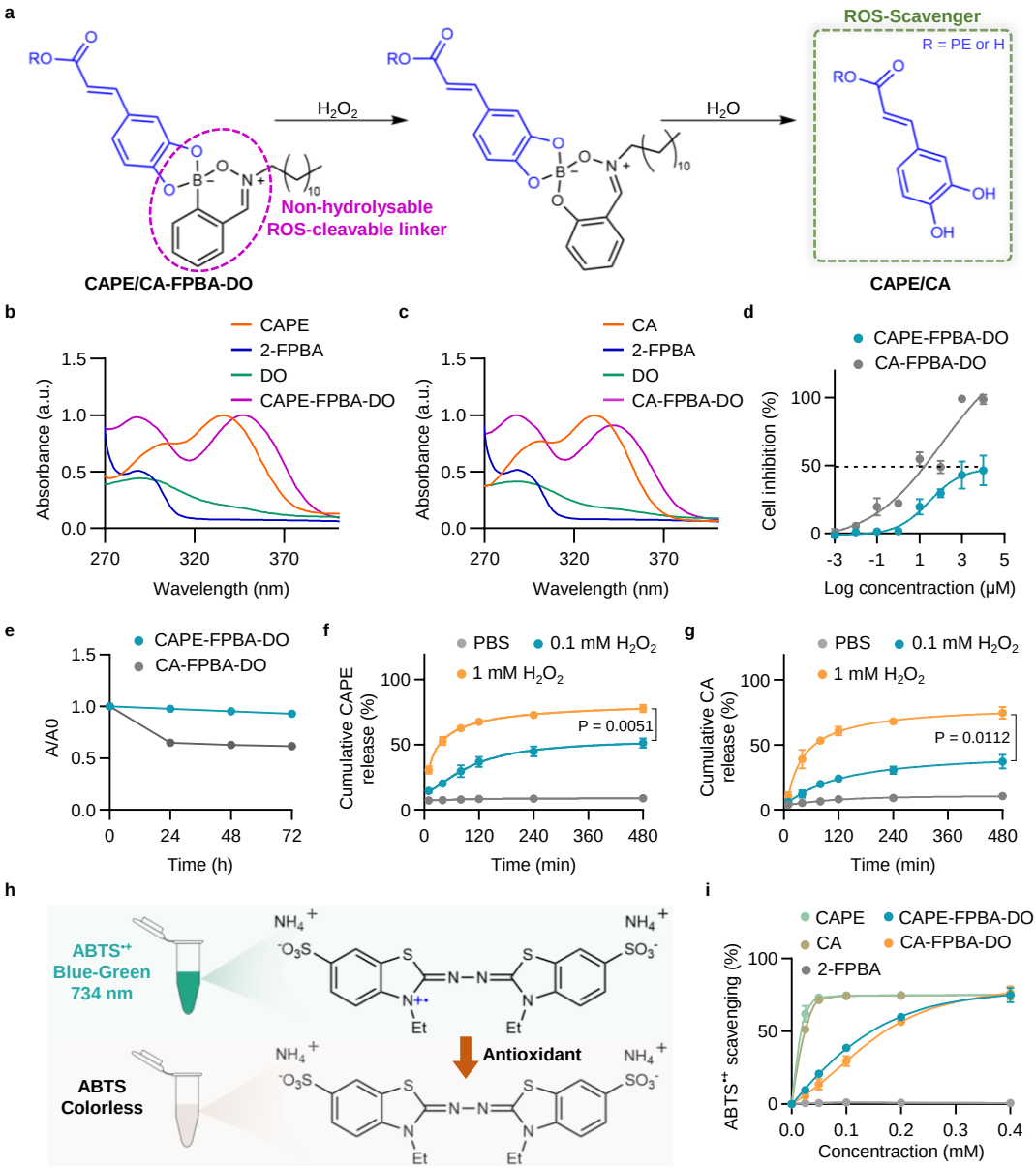
a
ROS-Scavenger
R = PE or H
H_2O_2
H_2O
Non-hydrolysable
ROS-cleavable linker
CAPE/CA-FPBA-DO
CAPE/CA
b
CAPE
2-FPBA
DO
CAPE-FPBA-DO
Absorbance (a.u.)
Wavelength (nm)
c
CA
2-FPBA
DO
CA-FPBA-DO
Absorbance (a.u.)
Wavelength (nm)
d
CAPE-FPBA-DO
CA-FPBA-DO
Cell inhibition (%)
Log concentration (μM)
e
CAPE-FPBA-DO
CA-FPBA-DO
A/A0
Time (h)
f
PBS
0.1 mM H_2O_2
1 mM H_2O_2
P = 0.0051
Cumulative CAPE release (%)
Time (min)
g
PBS
0.1 mM H_2O_2
1 mM H_2O_2
P = 0.0112
Cumulative CA release (%)
Time (min)
h
$ABTS^{\cdot+}$
Blue-Green
734 nm
ABTS
Colorless
Antioxidant
i
CAPE
CAPE-FPBA-DO
CA
CA-FPBA-DO
2-FPBA
$ABTS^{\cdot+}$ scavenging (%)
Concentration (mM)

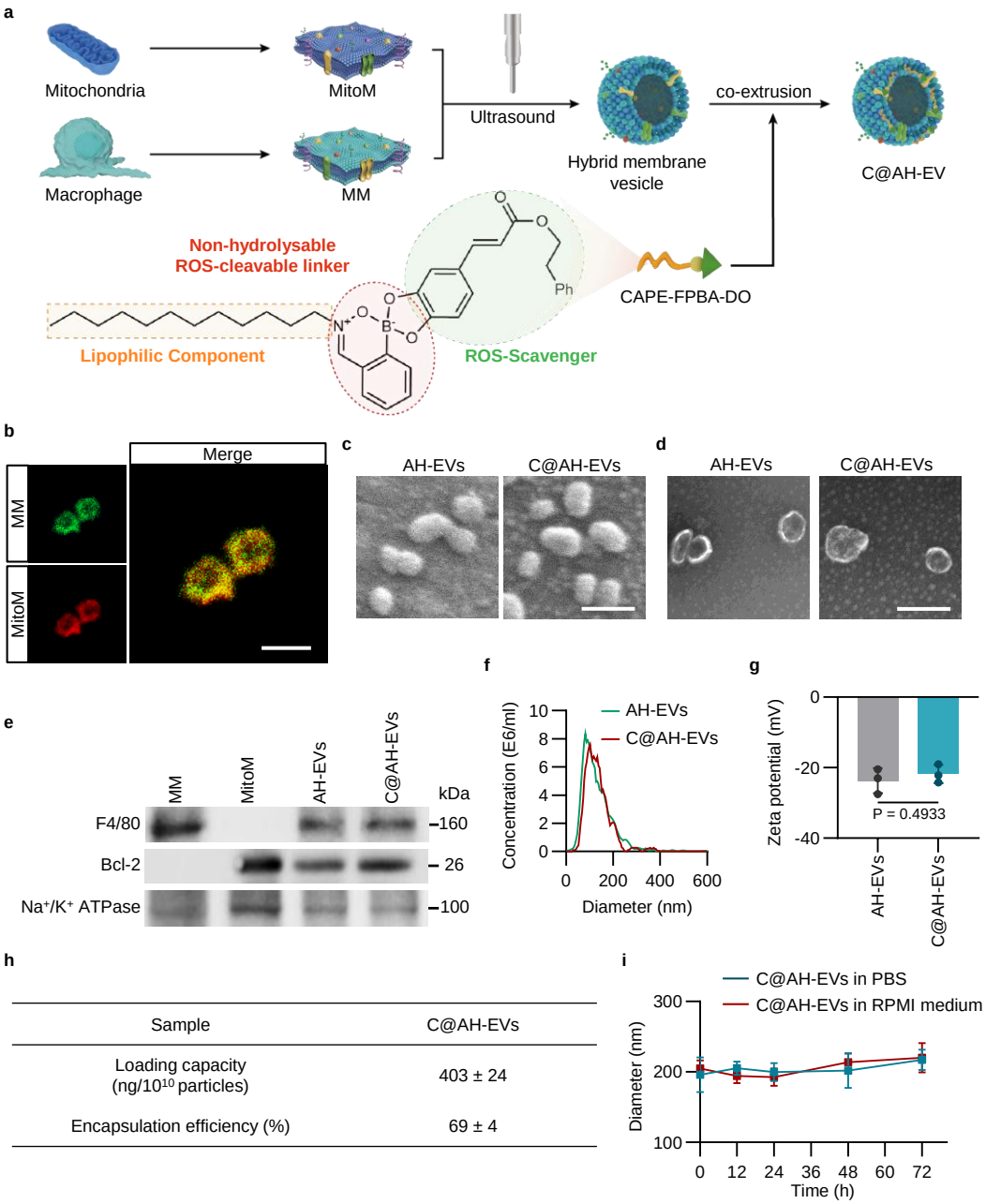

h

Sample	C@AH-EVs
Loading capacity ($ng/10^{10}$ particles)	403 ± 24
Encapsulation efficiency (%)	69 ± 4

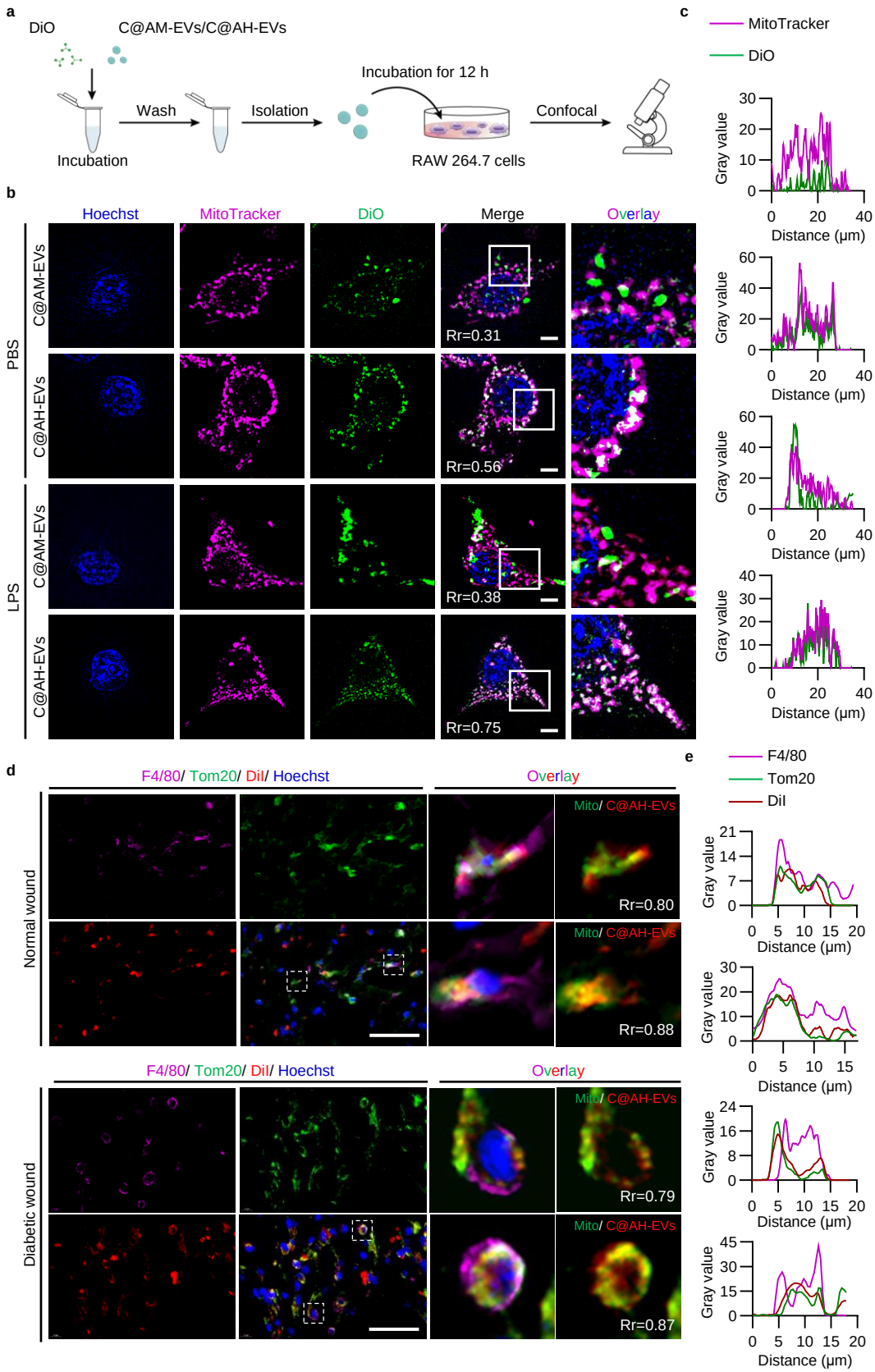
a
DiO
C@AM-EVs/C@AH-EVs
Incubation
Wash
Isolation
Incubation for 12 h
RAW 264.7 cells
Confocal
b
Hoechst
MitoTracker
DiO
Merge
Overlay
PBS
LPS
C@AM-EVs
C@AH-EVs
Rr=0.31
Rr=0.56
Rr=0.38
Rr=0.75
c
MitoTracker
DiO
Gray value
Distance (μm)
d
F4/80/ Tom20/ DiI/ Hoechst
Overlay
Mito/ C@AH-EVs
Normal wound
Diabetic wound
Rr=0.80
Rr=0.88
Rr=0.79
Rr=0.87
e
F4/80
Tom20
DiI
Gray value
Distance (μm)

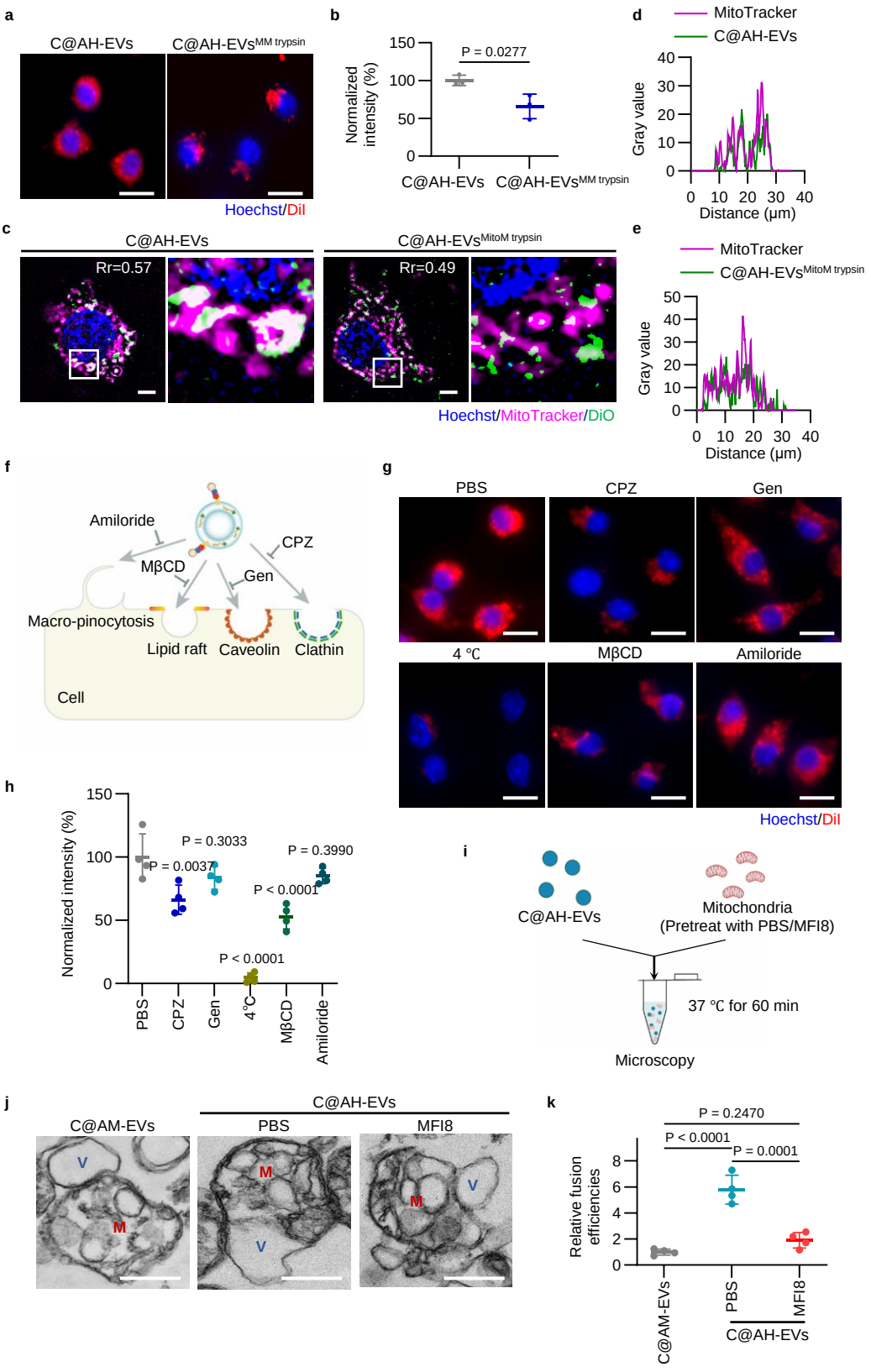
a
C@AH-EVs
C@AH-EVsMM trypsin
Hoechst/DiI
b
Normalized intensity (%)
P = 0.0277
C@AH-EVs
C@AH-EVsMM trypsin
d
MitoTracker
C@AH-EVs
Gray value
Distance (μm)
c
C@AH-EVs
C@AH-EVsMitoM trypsin
Rr=0.57
Rr=0.49
Hoechst/MitoTracker/DiO
e
MitoTracker
C@AH-EVsMitoM trypsin
Gray value
Distance (μm)
f
Amiloride
MβCD
CPZ
Gen
Macro-pinocytosis
Lipid raft
Caveolin
Clathin
Cell
g
PBS
CPZ
Gen
4 ℃
MβCD
Amiloride
Hoechst/DiI
h
Normalized intensity (%)
P = 0.3033
P = 0.0037
P = 0.3990
P < 0.0001
P < 0.0001
PBS
CPZ
Gen
4℃
MβCD
Amiloride
i
C@AH-EVs
Mitochondria
(Pretreat with PBS/MFI8)
37 ℃ for 60 min
Microscopy
j
C@AM-EVs
C@AH-EVs
PBS
MFI8
V
M
k
Relative fusion efficiencies
P = 0.2470
P < 0.0001
P = 0.0001
C@AM-EVs
PBS
MFI8
C@AH-EVs

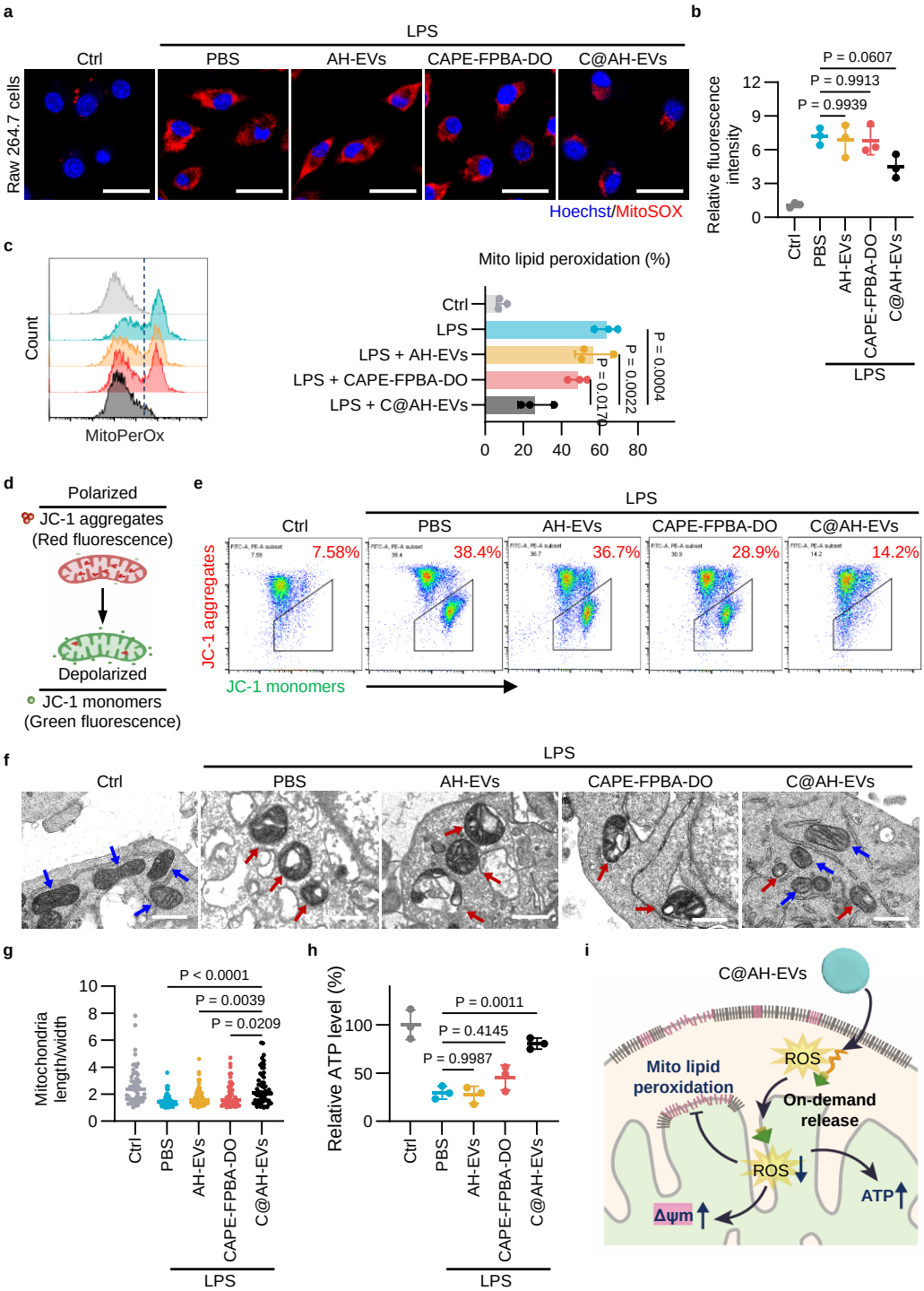
a
LPS
Ctrl
PBS
AH-EVs
CAPE-FPBA-DO
C@AH-EVs
Raw 264.7 cells
Hoechst/MitoSOX
b
Relative fluorescence intensity
P = 0.0607
P = 0.9913
P = 0.9939
Ctrl
PBS
AH-EVs
CAPE-FPBA-DO
C@AH-EVs
LPS
c
Count
MitoPerOx
Mito lipid peroxidation (%)
Ctrl
LPS
LPS + AH-EVs
LPS + CAPE-FPBA-DO
LPS + C@AH-EVs
P = 0.0004
P = 0.0022
P = 0.0170
d
Polarized
JC-1 aggregates
(Red fluorescence)
Depolarized
JC-1 monomers
(Green fluorescence)
e
LPS
Ctrl
PBS
AH-EVs
CAPE-FPBA-DO
C@AH-EVs
7.58%
38.4%
36.7%
28.9%
14.2%
JC-1 aggregates
JC-1 monomers
f
LPS
Ctrl
PBS
AH-EVs
CAPE-FPBA-DO
C@AH-EVs
g
Mitochondria length/width
P < 0.0001
P = 0.0039
P = 0.0209
Ctrl
PBS
AH-EVs
CAPE-FPBA-DO
C@AH-EVs
LPS
h
Relative ATP level (%)
P = 0.0011
P = 0.4145
P = 0.9987
Ctrl
PBS
AH-EVs
CAPE-FPBA-DO
C@AH-EVs
LPS
i
C@AH-EVs
Mito lipid peroxidation
ROS
On-demand release
ROS
ATP
Δψm

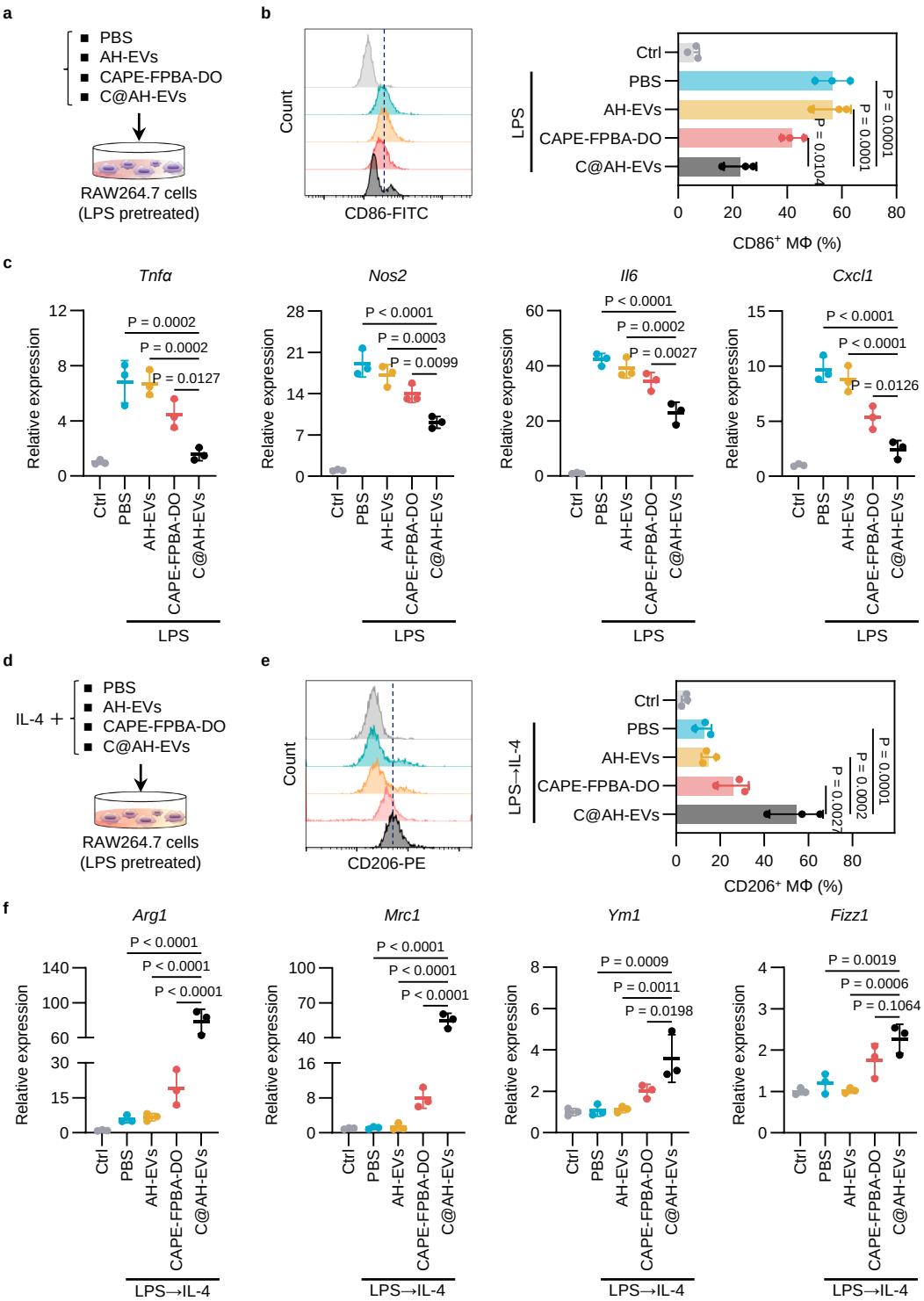
a
PBS
AH-EVs
CAPE-FPBA-DO
C@AH-EVs
RAW264.7 cells
(LPS pretreated)
b
Count
CD86-FITC
Ctrl
PBS
AH-EVs
CAPE-FPBA-DO
C@AH-EVs
LPS
P = 0.0001
P = 0.0001
P = 0.0104
0
20
40
60
80
CD86⁺ MΦ (%)
c
Tnfα
Nos2
Il6
Cxcl1
Relative expression
P = 0.0002
P = 0.0002
P = 0.0127
P < 0.0001
P = 0.0003
P = 0.0099
P < 0.0001
P = 0.0002
P = 0.0027
P < 0.0001
P < 0.0001
P = 0.0126
Ctrl
PBS
AH-EVs
CAPE-FPBA-DO
C@AH-EVs
LPS
d
IL-4 +
PBS
AH-EVs
CAPE-FPBA-DO
C@AH-EVs
RAW264.7 cells
(LPS pretreated)
e
Count
CD206-PE
Ctrl
PBS
AH-EVs
CAPE-FPBA-DO
C@AH-EVs
LPS→IL-4
P = 0.0001
P = 0.0002
P = 0.0027
0
20
40
60
80
CD206⁺ MΦ (%)
f
Arg1
Mrc1
Ym1
Fizz1
Relative expression
P < 0.0001
P < 0.0001
P < 0.0001
P < 0.0001
P < 0.0001
P < 0.0001
P = 0.0009
P = 0.0011
P = 0.0198
P = 0.0019
P = 0.0006
P = 0.1064
Ctrl
PBS
AH-EVs
CAPE-FPBA-DO
C@AH-EVs
LPS→IL-4

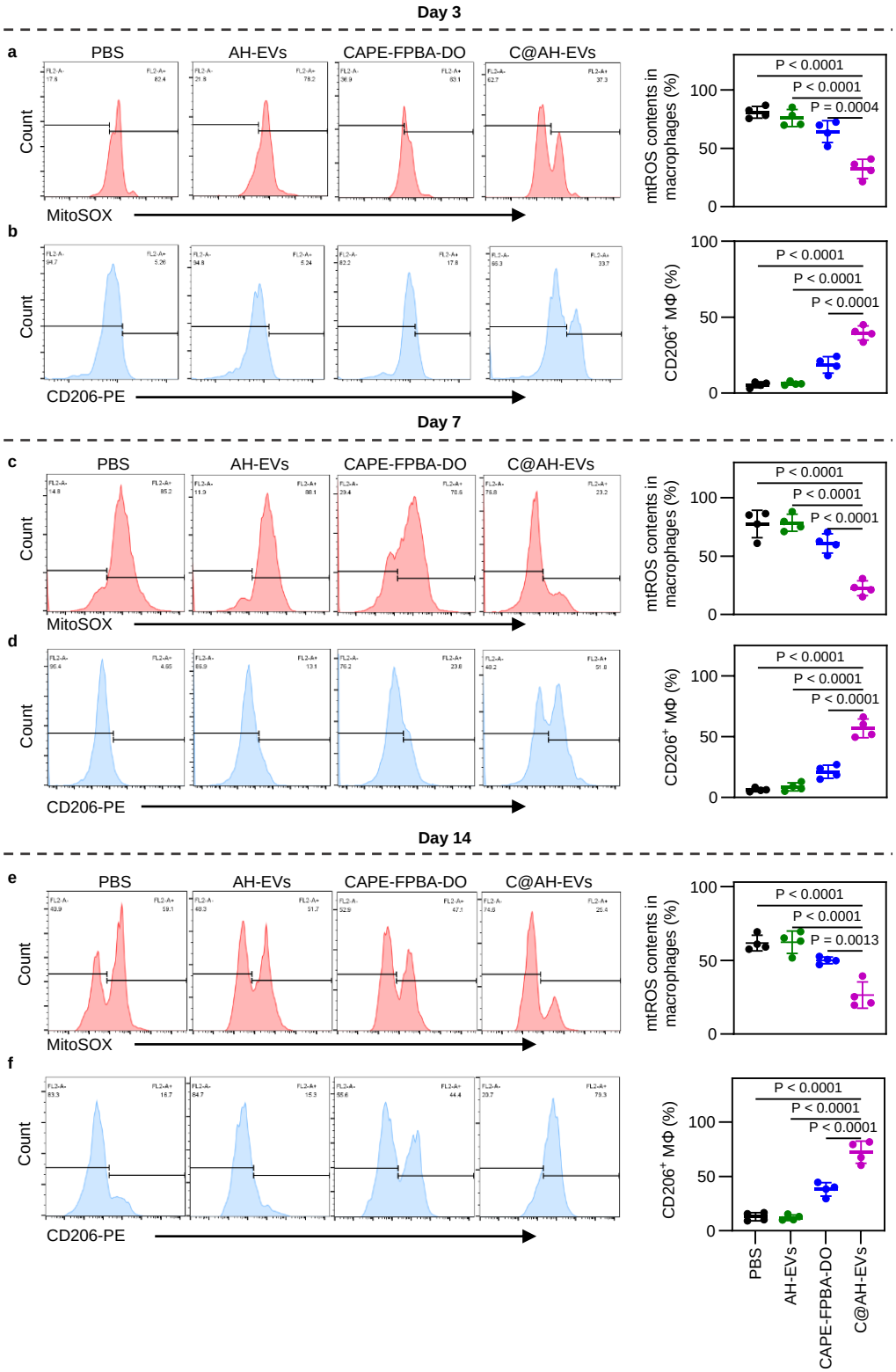
Day 3
a
PBS
AH-EVs
CAPE-FPBA-DO
C@AH-EVs
Count
MitoSOX
mtROS contents in macrophages (%)
P < 0.0001
P < 0.0001
P = 0.0004
b
CD206-PE
CD206+ MΦ (%)
P < 0.0001
P < 0.0001
P < 0.0001
Day 7
c
MitoSOX
P < 0.0001
P < 0.0001
P < 0.0001
d
CD206-PE
P < 0.0001
P < 0.0001
P < 0.0001
Day 14
e
MitoSOX
P < 0.0001
P < 0.0001
P = 0.0013
f
CD206-PE
P < 0.0001
P < 0.0001
P < 0.0001
PBS
AH-EVs
CAPE-FPBA-DO
C@AH-EVs

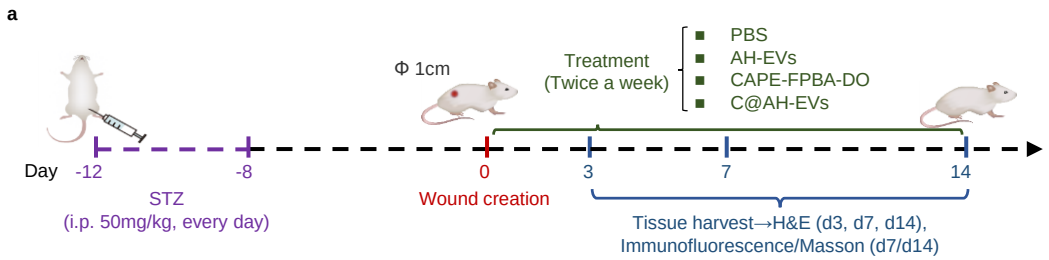
a
Φ 1cm
Treatment
(Twice a week)
PBS
AH-EVs
CAPE-FPBA-DO
C@AH-EVs
Day -12 -8 0 3 7 14
STZ
(i.p. 50mg/kg, every day)
Wound creation
Tissue harvest→H&E (d3, d7, d14),
Immunofluorescence/Masson (d7/d14)

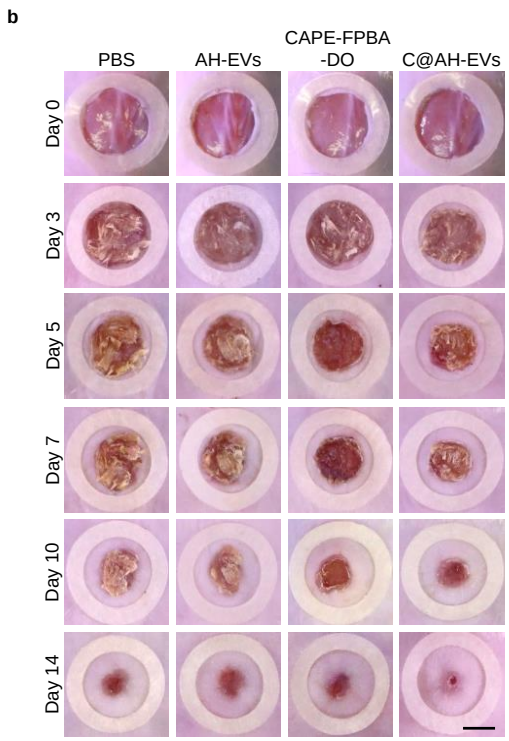
b
PBS
AH-EVs
CAPE-FPBA
-DO
C@AH-EVs
Day 0
Day 3
Day 5
Day 7
Day 10
Day 14

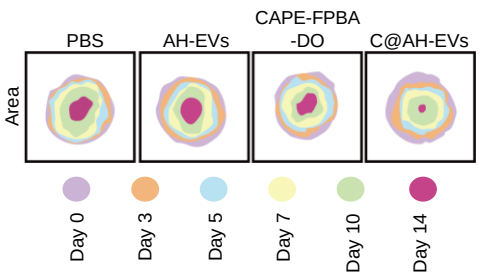
c
PBS
AH-EVs
CAPE-FPBA
-DO
C@AH-EVs
Area
Day 0
Day 3
Day 5
Day 7
Day 10
Day 14

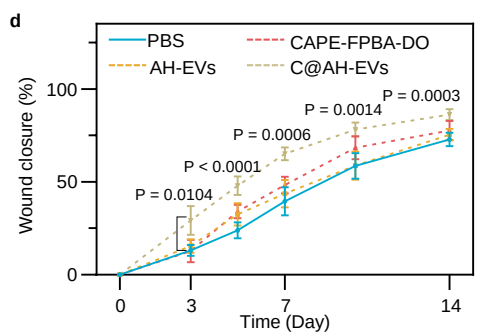
d
PBS
AH-EVs
CAPE-FPBA-DO
C@AH-EVs
Wound closure (%)
100
50
0
P = 0.0104
P < 0.0001
P = 0.0006
P = 0.0014
P = 0.0003
0
3
7
14
Time (Day)

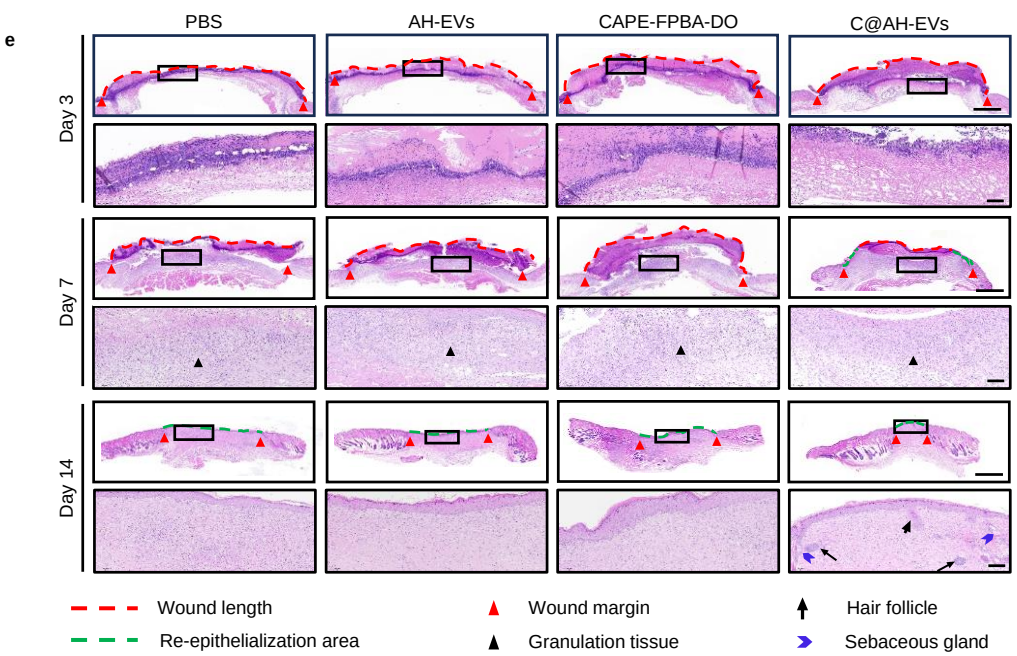
e
PBS
AH-EVs
CAPE-FPBA-DO
C@AH-EVs
Day 3
Day 7
Day 14
Wound length
Re-epithelialization area
Wound margin
Granulation tissue
Hair follicle
Sebaceous gland